Biophysical Chemistry 320–321 (2025) 107410

Contents lists available at ScienceDirect

Biophysical Chemistry

journal homepage: www.elsevier.com/locate/biophyschem

Targeting human prostaglandin reductase 1 with Licochalcone A: Insights from molecular dynamics and covalent docking studies

Sara Abigail Ramírez-Cortés [a,1], Adrián Durán-Vargas [a,1], Jesús Antonio Rauda-Ceja [a], Paola Mendoza-Espinosa [a], Luis Fernando Cofas-Vargas [b], Armando Cruz-Rangel [c], Julio Isael Pérez-Carreón [d], Enrique García-Hernández [a,*]

[a] Universidad Nacional Autónoma de México, Instituto de Química, Ciudad Universitaria, Ciudad de Mexico, 04510, Mexico
[b] Biosystems and Soft Matter Division, Institute of Fundamental Technological Research, Polish Academy of Sciences, Pawińskiego 5B, 02-106 Warsaw, Poland
[c] Biochemistry of Chronic Diseases Laboratory, National Institute of Genomic Medicine, INMEGEN, Mexico City, Mexico
[d] Laboratory of Liver Diseases, National Institute of Genomic Medicine, INMEGEN, Mexico City, Mexico

ARTICLE INFO

Keywords:
Leukotriene B4 dehydrogenase
NADPH-dependent enzyme
Molecular dynamics simulation
Covalent inhibition
Specific target for cancer therapy

ABSTRACT

Prostaglandin reductase 1 (PTGR1) is an NADPH-dependent enzyme critical to eicosanoid metabolism. Its elevated expression in malignant tumors often correlates with poor prognosis due to its role in protecting cells against reactive oxygen species. This study explores the inhibitory potential of licochalcone A, a flavonoid derived from Xinjiang licorice root, on human PTGR1. Using molecular dynamics simulations, we mapped the enzyme's conformational landscape, revealing a low-energy, rigid-body-like movement of the catalytic domain relative to the nucleotide-binding domain that governs PTGR1's transition between open and closed states. Simulations of NADPH-depleted dimer and NADPH-bound monomer highlighted the critical role of intersubunit interactions and coenzyme binding in defining PTGR1's conformational landscape, offering a deeper understanding of its functional adaptability as a holo-homodimer. Covalent docking, informed by prior chemoproteomic cross-linking data, revealed a highly favorable binding pose for licochalcone A at the NADPH-binding site. This pose aligned with a transient noncovalent binding pose inferred from solvent site-guided molecular docking, emphasizing the stereochemical complementarity of the coenzyme-binding site to licochalcone A. Sequence analysis across PTGR1 orthologs in vertebrates and exploration of 3D structures of human NADPH-binding proteins further underscore the potential of the coenzyme-binding site as a scaffold for developing PTGR1-specific inhibitors, positioning licochalcone A as a promising lead compound.

1. Introduction

Prostaglandins are a group of lipid molecules derived from arachidonic acid through the action of cyclooxygenases. Functioning locally as messenger molecules, they play pivotal roles in various physiological processes. These include inflammation, cell survival, apoptosis, regulation of smooth muscle contraction, adipocyte differentiation, vasodilation, and the inhibition of platelet aggregation [1]. Prostaglandin reductases (PTGR) are key enzymes in the irreversible inactivation of these eicosanoids and are zinc-independent members of the medium-chain dehydrogenase/reductase (MDR) superfamily [2].

PTGR1, originally identified as leukotriene B4 dehydrogenase [3], is a rate-limiting enzyme involved in the arachidonic acid pathway. This enzyme is an NADPH-dependent alkenal/one oxidoreductase, that catalyzes the reduction of double bonds in α/β-unsaturated ketones, alkenals, and nitroalkenes [4]. Its primary role involves the deactivation of certain eicosanoids [4]. Among its main substrates are lipoxin A4, prostaglandin E2, and leukotriene B4. Recent studies have indicated its involvement in further metabolizing eicosanoids through both the cyclooxygenase and lipoxygenase downstream pathways [5]. Structurally, it exhibits the alcohol dehydrogenase fold characteristic of the MDR superfamily [6]. Each monomer comprises a catalytic domain and a nucleotide-binding Rossmann domain [7–10]. Fig. 1 illustrates a model of the structural organization of the human PTGR1 dimer bound to NADPH and the metabolite 15-oxo-prostaglandin E2. Each subunit contains an NADPH molecule embedded in a deep cavity formed by the

* Corresponding author.
E-mail address: egarciah@unam.mx (E. García-Hernández).
[1] These authors contributed the same.

https://doi.org/10.1016/j.bpc.2025.107410
Received 13 September 2024; Received in revised form 28 January 2025; Accepted 11 February 2025
Available online 14 February 2025

catalytic (residues 1–122 and 297–329) and NADPH-binding (residues 123–276) domains. The catalytic site resides in a cavity bordered at its base by NADPH and flanked by residues from both subunits, highlighting the essential role of the homooligomeric state in the function of most MDR enzymes [11–13].

The NADPH-dependent alkenal oxide reductase activity of PTGR1 is pivotal in irreversibly inactivating multiple eicosanoids associated with the inflammatory response [15]. Additionally, its activity supports the reduction of polyunsaturated fatty acids susceptible to lipoperoxidation by reactive oxygen species. Consequently, PTGR1 is recognized as a vital component of the cellular detoxification system [16]. Numerous studies consistently demonstrate a correlation between the overexpression of PTGR1 in diverse cancer types (such as liver, lung, prostate, and bladder) and an unfavorable prognosis for patient survival [17–20]. On the contrary, diminished PTGR1 expression is linked to unfavorable prognosis in ovarian, endometrial, and kidney cancers [4]. This dual role positions PTGR1 as a potential selective marker for prognosis and treatment guidance. Moreover, suppressing PTGR1 through short hairpin RNA molecules in triple-negative breast cancer cells (TNBC) leads to reduced cell proliferation [21]. In prostate cancer cell lines, silencing PTGR1 expression induces cell cycle arrest in the G0/G1 phase, accompanied by a decrease in cyclin D1 and an increase in apoptosis markers [19]. In induced hepatocellular carcinoma cellular models, PTGR1 exhibits a progressive increase in expression from early to advanced stages of hepatocellular carcinoma development. Notably, persistent nodules with elevated PTGR1 expression display heightened cell proliferation and enhanced resistance to oxidative stress. This resistance is attributed to PTGR1's conversion activity on lipoperoxidation-derived products, such as 4-hydroxy-trans-nonenal [17]. Consequently, the accumulated evidence supports PTGR1's oncogenic role, rendering it an appealing target for the exploration and development of molecules to inhibit its activity.

Although PTGR1 stands as a promising therapeutic target for cancer therapy, the availability of inhibitors for this enzyme remains limited. Several studies have identified specific nonsteroidal anti-inflammatory drugs like indomethacin, niflumic acid, and diclofenac as effective inhibitors of PTGR1 [2,22]. Among these, indomethacin exhibited the highest inhibitory effect, with more than 95 % inhibition and an IC_{50} of 8.7 μM, whereas niflumic acid demonstrated ~80 % inhibition with an IC_{50} of 7.1 μM [1,22]. Licochalcone A (LicA) is a flavonoid obtained from Xinjiang licorice root with antiparasitic, antibacterial, and antitumor properties [23,24]. The antitumor effects of LicA are correlated with the induction of apoptosis via the inhibition of PI3K/Akt/mTOR signaling pathway in HepG2 cells [25]. Treatment with LicA in H460 and A549 cells demonstrated a dose-dependent inhibition of the expression of cell cycle-related genes, including MDM2, Cyclin B1, and Cdc2. This led to the suppression of proliferation, linked with G2/M phase arrest [26]. In addition, LicA inhibited the growth of TNBC with an IC_{50} of 8.4 μM. By employing chemoproteomic profiling techniques, LicA was found to disrupt the pathogenicity of TNBC by inhibiting PTGR1 [27].

Although it has been proposed that LicA might serve as a potential PTGR1 inhibitor, there is currently a lack of information regarding its inhibitory activity or structural studies detailing its interaction with PTGR1. In this study, we aimed to characterize the conformational landscape of PTGR1 by molecular dynamics (MD) simulations. Our data revealed a plausible mechanism driving the enzyme's transition between open and closed states. To investigate the effects of NADPH

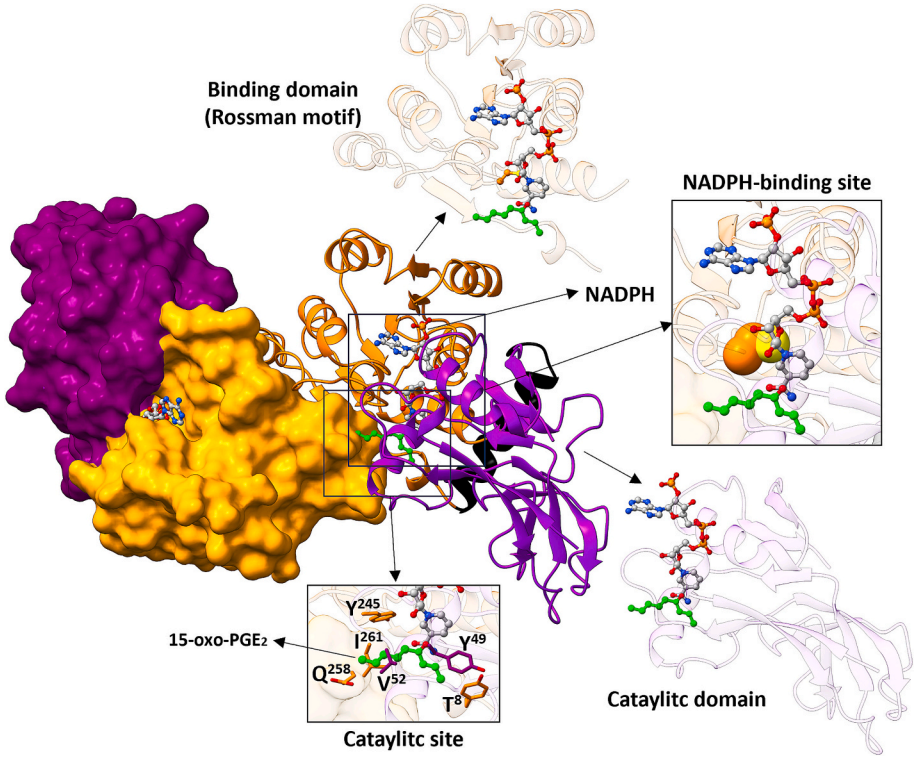

Fig. 1. Molecular model of the human PTGR1 dimer bound to NADPH and a substrate. The holo form of human PTGR1 was constructed by aligning two monomers, each bound to NADPH and the inhibitor raloxifene (PDB ID 2Y05), to the apo dimer structure (PDB ID 1ZSV). The guinea pig PTGR1 dimer structure (PDB ID 1V3V [14]) was used to position the solved moiety of the metabolite 15-oxo-prostaglandin E2, overlapping the raloxifene binding site This substrate orientation closely matchs with the binding pose obtained via docking to the human enzyme, as detailed in reference [1]. Insets provide close-up views of the catalytic and NADPH-binding sites, as well as structural delineations of the catalytic domain (residues 1–122, 297–329) and the NADPH-binding domain (residues 123–276). The small hinge domain (residues 277–296), identified in this study as critical for conformational transitions, is highlighted in black. NADPH and 15-oxo-prostaglandin E2 are shown in gray and green sticks, respectively. (For interpretation of the references to color in this figure legend, the reader is referred to the web version of this article.)

binding and the oligomeric state on the conformational landscape of the holo dimer, additional simulations were conducted for the apo dimer and the NADPH-bound monomeric subunit. Guided by prior reported experimental cross-linking data [27], we derived a covalent binding pose for the inhibitor at the nucleotide-binding site and examined the conformational effects induced by this adduct formation. Finally, an analysis of NADPH-binding protein sequences and 3D structures highlighted LicA as a promising scaffold for developing drug-like inhibitors selectively targeting PTGR1, providing a potential strategy to combat malignant cells.

2. Methods

2.1. Molecular dynamics simulations

Two structures of human PTGR1 have been deposited in the PDB: one bound to NADPH and the raloxifene inhibitor (PDB ID 2Y05, 2.2 Å resolution), and another in apo form (PDB ID 1ZSV, 2.3 Å resolution). In the first structure, it is reported as a monomer, whereas in the second as a dimer. However, the protomers exhibit highly similar conformations in both structures (backbone RMSD ~0.5 Å). Experimental evidence, akin to PTGR1 orthologs and many other MDR enzymes, indicates that the functional form of human PTGR1 is a homodimer [1]. Thus, to construct the dimeric form of the coenzyme complex, we duplicated the NADPH-bound protomer from 2Y05 and aligned the two subunits with the dimer from 1ZSV, deleting the raloxifene molecule. In the resulting structure, no steric clashes were observed between the protomers, making it suitable as the starting point for the simulations. Additionally, the apo dimer was generated by removing the NADPH from both subunits, while the monomeric form in complex with NADPH was derived from the corresponding crystal structure (PDB ID 2Y05).

The pmemd.cuda module of AMBER 22 was used to perform the MD simulations, employing the force field FF19SB and the OPC water model [28–31]. NADPH parameters were taken from [32]. The system was protonated at pH 7.4 with PDBfixer [33] and placed in a truncated octahedral box, initially spanning 12 Å further from the solute in each direction using the AMBER tLeap module. The overall charge of the system was neutralized by the addition of four sodium ions. ParmEd [34] was used to implement the hydrogen mass repartitioning scheme [35]. Local clashes and solvent orientation were corrected using the steepest descent algorithm for 5000 cycles. During the initial NVT equilibration, the velocities gradually increased through five steps of 200 ps each. The temperature progression started at 150 K and was raised to 200 K, 250 K, 300 K, and finally, 310 K. Position restraints were applied to heavy atoms of the protein, with the restraining forces progressively decreasing at each step. The spring constants were set at 4, 5, 3, and 1 kcal/mol $Å^2$, respectively, to allow for the gradual relaxation of the protein. The system was further equilibrated for 1 ns in the NPT ensemble with no restraints. For treating long-range electrostatic interactions, periodic boundary conditions and Ewald sums were used with a 9 Å cutoff for direct interactions [36,37]. The same cutoff was used for Lennard-Jones interactions. The Langevin thermostat [38] with a collision frequency of 4 ps^{-1} and the Monte Carlo barostat [39] with a pressure relaxation time of 2 ps were used to control temperatures and pressures, respectively. The SHAKE algorithm was used to fix any bond involving hydrogen atoms [40], and a 4-fs time step integration was used [41,42] Unless otherwise stated, no other constraints were used. Five replicas of 500 ns each per system were produced.

The topology and parameter files for a LicA molecule and for this inhibitor covalently bound to the sulfur atom of a cysteine residue were generated with Antechamber suite [43], using the general Amber force field (GAFF2) for organic molecules [44]. Atomic charges were derived using the AM1-BB method [45]. The parameters are documented in Supplementary Tables SI-1 and SI-2. Trajectories for PTGR1 covalently and noncovalently bound to LicA were run using the same conditions as described above. All molecular structure representations were created using UCSF ChimeraX v1.8 [46,47].

2.2. MD trajectory analysis

Structural analysis was performed using CPPTRAJ [48]. It included autocorrelation, hydrogen bonds (HB), intermolecular contacts, radius of gyration (RoG), root-mean-square deviation (RMSD), and principal component analysis (PCA). Data analysis and visualization plots were created with the Python libraries Pandas [49], Matplotlib [50] and Seaborn [51]. The flexibility of the protein was evaluated using the MDLovofit program, which determines regions with the lowest RMSD value to be used as the aligning mask for all trajectory conformers [52].

2.3. Characterization of domain-domain displacements

To characterize domain motion in PTGR1, the most divergent conformations relative to the reference structure were identified in the MD trajectories. The closed (experimental) and the selected most open conformers were examined using the DynDom software [53]. By comparing these extreme conformations, the inter-domain screw axes and inter-domain bending regions were determined.

2.4. Dynamic cross-correlation analysis

The displacement of each Cα atom in the subunits was evaluated to quantify the extent of their correlated motions. The degree of dynamic cross-correlation between pairs of atoms was determined by calculating the covariance of their pairwise fluctuations [54]. The cross-correlation coefficient *c(i,j)* was calculated using the following equation:

$$c(i,j) = \frac{\langle \Delta r_i \cdot \Delta r_j \rangle}{\langle \Delta r_i^2 \rangle^{1/2} \cdot \langle \Delta r_j^2 \rangle^{1/2}} \quad (1)$$

where Δr_i and Δr_j are the ensemble average displacement vectors of atoms i and j, respectively, averaged over the ensemble of configurations. A positive correlation (values close to +1) indicates that the atoms move in the same direction, whereas a negative correlation (values near −1) reflects anticorrelated motion, meaning that the atoms tend to move in opposite directions. A coefficient close to zero indicates a lack of correlation, signifying that the motions of the two atoms are independent [55].

2.5. Cartesian principal component analysis

PCA was applied to MD trajectories to reduce the data dimensionality and identify a set of orthogonal principal components, each representing dominant modes trends of the protein's collective motions [56]. This method simplifies the complex data by capturing the most significant conformational changes across multiple dimensions. For each system, a combined trajectory was generated that combined by concatenating the data for the last 350 ns of the five replicates for both subunits taken together. To specifically highlight the displacement of the catalytic domain relative to the NADPH-binding domain, the concatenated trajectory was aligned to the latter domain (residues 123–276). Next, from this aligned trajectory, the 3 N covariance matrix was calculated, where N represents the number of atoms in the protein. The covariance matrix captures the degree of correlated motion between pairs of atomic coordinates over time. The matrix was then decomposed by diagonalization, a step that removes instantaneous linear correlations between variables and yields the eigenvectors and eigenvalues. Eigenvectors define the principal components (PCs), or directions of motion, while the eigenvalues correspond to the amplitude of movement along each PC. To prioritize the most significant motions, eigenvalues were sorted in descending order.

To further explore these dominant motions, two-dimensional free

energy landscapes (FEL) were constructed using the first two principal components, PC1 and PC2, with PyEMMA [57]:

$$G(x) = -k_B{*}T{*}lnP(x) \quad (2)$$

where $G(x)$ is the x-coordinate free energy landscape, k_B is the Boltzmann constant, T is the absolute temperature and $P(x)$ represents the probability distribution of positions along PC1 and PC2, represented as a two-dimensional histogram. This landscape reveals conformational preferences and transitions, providing a visual map of the most accessible energy states in the protein's dynamic behavior.

2.6. Solvent-site identification and guided docking

Determination of solvent sites (SS) for ethanol and water molecules was conducted by employing the MDmix method. After removing both NADPH molecules from the enzyme dimer, the system was protonated at pH 7.4 with PDBfixer [33] and placed in a truncated octahedral box of water/ethanol 80/20 % *v*/v, extending 12 Å beyond the solute in each direction using the AMBER tLeap module. Five 20 ns replicas were run, using the same conditions described above, but applying Cartesian restrictions of 0.01 kcal/mol A^2 over all heavy atoms. After the alignment of trajectories, density maps for probe atoms were generated by constructing a static mesh with cubic grids (0.5 Å edge length) over the entire simulation box. The occurrence of probe atoms within each grid were tracked across the trajectories. These density distributions were then converted into binding free energy using the Boltzmann relationship, comparing observed probe atom distributions against the expected bulk solvent distribution at 1.0 M. Solvent sites were then filtered by applying an energy threshold of −1 kcal/mol [58,59].

2.7. LicA docking

For covalent docking, LicA, bound through its C_β atom to the sulfur atom of C^{239}, was docked onto the NADPH-binding site of human PTGR1 employing the covalent docking module of AutoDock4 v4.2.6 [60,61]. The flexible side-chain methodology was used. For noncovalent docking, solvent sites for ethanol and water molecules were used as pharmacophoric elements for rDock [62]. This docking involved defining the receptor system and generating a binding cavity using NADPH as a reference molecule. During the noncovalent docking, a penalty score proportional to the square of the distance from each ligand conformation to a solvent site was applied when the separation exceeded 2 Å. The docking run included 100 simulations, generating a set of potential binding modes for LicA within the NADPH-binding site site.

2.8. Sequence analysis of NADPH-binding sites

Sequences of vertebrate PTGR1 orthologs were retrieved from the UniProt database [63]. Unreviewed entries were excluded. A multiple alignment of 530 sequences was generated employing Clustal Omega [64]. Furthermore, sequences of human NADPH-binding proteins with experimentally determined 3D structures were compiled. Subsequently, sequence logos corresponding to the nucleotide-binding residues for each protein dataset were created using the Weblogo3 server [33].

3. Results

3.1. Conformational flexibility of PTGR1

To unveil the conformational landscape of PTGR1, we characterized the enzyme dimer bound to two NADPH molecules using unconstrained MD simulations. Five replicates of 500 ns each were generated at 310 K, pH 7.4, under NPT conditions. According to an autocorrelation analysis of backbone dihedral angles, all replicas achieved independence from the starting coordinates within the first 150 ns (Fig. SI-1). Conformational relaxation was evident during this period as well, as reflected in the RMSD and RoG trends (Fig. SI-2). Therefore, for the subsequent analysis, only the last 350 ns of the trajectories were considered. These five partial trajectories were concatenated into a single trajectory to perform a global analysis of the data.

RMSD and RoG analyses of the PTGR1dimer revealed complex dynamic behaviors associated with significant conformational changes. The RMSD histogram depicted a broad distribution (~5 Å), with a primary peak centered at ~2.5 Å (Fig. SI-2 A). These conformers clustered into two similarly populated groups with different degrees of compactness, as indicated by the RoG histograms (Fig. SI-2B). To clarify the origin of these conformational variations, self-alignments of the catalytic (residues 1–122, 297–329) and the nucleotide-binding (residues 123–276) domains were performed. For this analysis, each protomer was individually isolated, and the ten resulting 350-ns trajectories were combined into a single trajectory. As shown in Fig. 2A, each domain exhibited a narrow, unimodal probability distribution centered at an RMSD value of ~1 Å. Consistent with this, the catalytic and NADPH-binding domains preserved conformations nearly superimposable throughout the trajectory (Fig. 2B). These results indicate that each domain behaved as a single structural entity. The region comprising residues 277–296, which serves as a connector between the catalytic and nucleotide-binding domains, exhibited only marginal conformational variation.

The results presented suggest that the overall conformational fluctuations of PTGR1 arise from rigid body-like displacements between domains. To characterize these displacements, trajectories aligned to the nucleotide-binding domain were analyzed using Cartesian PCA. The analysis revealed that the main principal component describes a concerted movement of the catalytic domain relative to the nucleotide-binding domain (Fig. 3A). In contrast, the connecting domain exhibited minimal changes, consistent with a hinge-like functionality, suggesting it facilitates the observed domain displacements. Similar results were obtained when the catalytic domain was used as alignment reference (data not shown). Analysis of RMSD revealed that the positional shift of the catalytic domain relative to the nucleotide-binding domain ranged mostly between 2 and 5 Å (Fig. 3B). However, transient conformations with RMSD values up to 15 Å were observed, where NADPH, while maintaining a pose similar to the reference one, largely lost contact with the catalytic domain (Fig. 3C). To further describe the enzyme's opening, the angle between two vectors was defined (Fig. 3D). The angle probability densities described a pattern similar to that in Fig. 3B, featuring a predominant peak at ~17.5° and a less populated one at ~23.5°. A strong correlation ($r = 0.92$) was observed between the RMSD and rotation angle values (Fig. 3E), showing that both metrics effectively captured the enzyme's conformational rearrangement. The most open conformations can be attributed to a hinge-like motion between two rigid bodies, with an axis of rotation around the α-helix formed by residues 277–292 and a maximum angle change of ~35° [65]. This approach pinpointed the same segment previously identified in the RMSF and RMSD analyses (Fig. 2), albeit shortened by four residues. The opening angle was accompanied by a rotameric change of the φ angle of K^{299}, albeit with a weak correlation between the two angles ($r = -0.47$). Additionally, the ϕ angle of K^{299} and the φ angle of Y^{298} displayed significant rotameric differences between the closed and most open states. However, these changes showed no quantitative correlation with the open movement of the two domains.

To quantify the relative abundance of PTGR1 conformations, free energy landscapes (FEL) were constructed from the Cartesian PCA of the enzyme-coenzyme complex (Fig. 4). The FEL displayed a prominent basin representing the most stable conformation, along with two shallower basins that indicate the presence of less-stable conformations (Fig. 4A). In alignment with the coordinated motion depicted by the projection of conformers onto the PC1 eigenvector (Fig. 3A), the first component accounted for 64 % of the total variance in the trajectory (Fig. 4A's inset), underscoring its role in the enzyme's primary

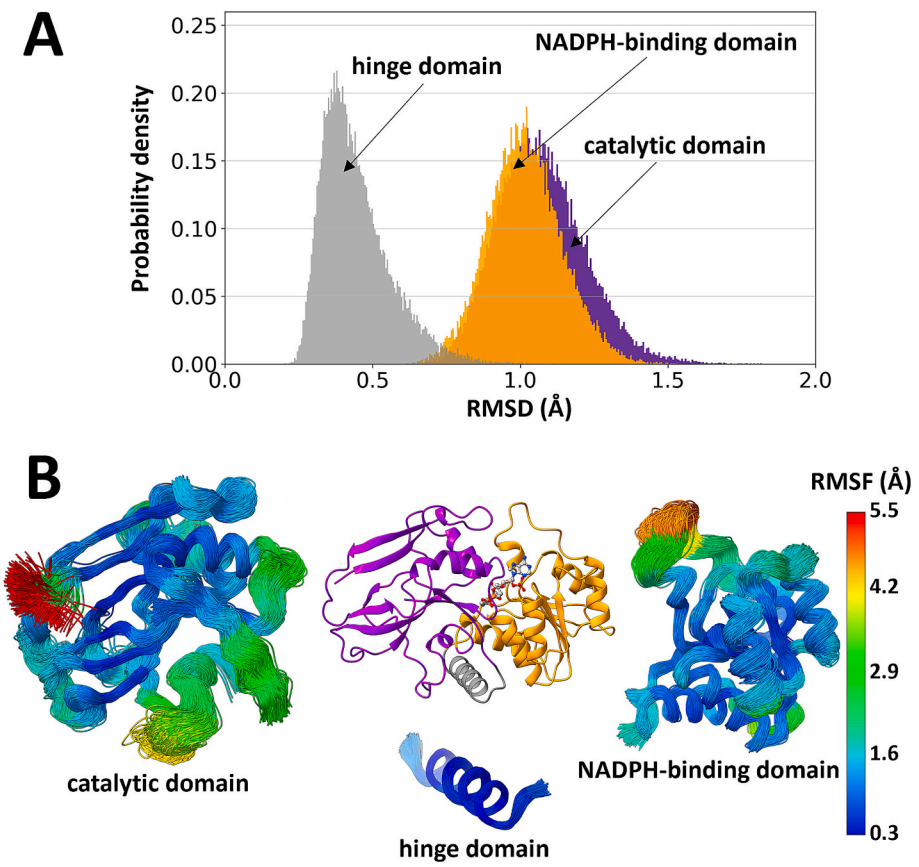

Fig. 2. Conformational flexibility of PTGR1 in complex with NADPH. **(A)** RMSD probability densities of the catalytic (residues 1–122, 297–329), NADPH-binding (residues 123–276), and hinge (residues 277–298) domains, calculated relative to the initial structure. **(B)** Snapshots extracted from the MD trajectories, taken every 50 ns, optimally aligned using residues of the corresponding domain with the lowest RMSD (< 0.8 Å) and the highest residue coverage fraction (> 0.7) [52]. Snapshots are color-coded according to RMSF values (Å) of backbone heavy atoms, as shown on the color scale. The corresponding RMSF plot is shown in Fig. SI-3. Data represents a combined analysis of both PTGR1 protomers over the last 350 ns from five replicate simulations at 310 K, pH 7.4.

conformational changes. A clustering analysis provided further insights into the enzyme's conformational dynamics, pinpointing three distinct states within the FEL (Fig. 4A). The most probable state, S1, represented a closed PTRG1 conformation. The remaining, less-populated states corresponded to conformations with differing degrees of NADPH-binding site accessibility (Fig. 4B). Notably, tracking transitions between conformational clusters revealed that the most open conformation, S3 (with a relative abundance of 0.11), is accessible from S1 (relative abundance of 0.71) only through a sequential pathway in which the semi-open state S2 (relative abundance of 0.18) functions as an obligatory intermediate. These findings highlight the simulations' effectiveness in capturing the sequential transitions integral to the enzyme's opening mechanism, offering valuable insights into its structural adaptability and the stepwise nature of its conformational shifts.

To investigate interaction changes associated with the PTGR1 conformational groups, we analyzed contact frequencies in each state (Table SI-1). Fig. 5 highlights contacts with prevalence shifts > |0.5| when comparing the open states S2 and S3 relative to the closed state S1. A progressive opening pathway was observed, propagating from the mouth to the base of the NADPH-binding cavity. This is reflected in the increasing number of disrupted contacts from S1 → S2 (19 broken contacts) to S1 → S3 (27 broken contacts). The simulations showed that only three intradomain persistent hydrogen bonds in S1 were lost in both S2 and S3 (G^{15}:R^{51}, P^{48}:R^{51}, Y^{245}:I^{242}). Thus, the enzyme opening was largely coupled to the loss of interdomain nonpolar interactions. Concurrently, new intradomain contacts formed in S2 (5 contacts) and S3 (13 contacts). Driven by local repositioning of the secondary structure in S3 relative to S1, two intradomain hydrogen bonds (T^{121}:E^{300}, P^{48}:R^{51}) and two salt bridges (T^{45}:Q^{66}) were established. Overall, these findings highlight a stepwise mechanism for cavity opening that propagates from the mouth to the bottom of the NADPH-binding cavity, which may be critical for coenzyme binding and release.

Throughout the simulations, a total of 20 residues engaged in direct interactions with NADPH with a cumulative frequency > 0.7 (Fig. SI-4). In line with the results indicating that the coenzyme stayed anchored to the nucleotide-binding domain regardless of the opening state of the binding site, three out of four contacting residues belonged to the last domain. Moreover, four distinctive enzyme-coenzyme hydrogen bonds were identified, each mediated by a phosphate moiety of NADPH. The peptide bonds of A^{153} and G^{174}, as well as the side chains of K^{178} and K^{324}, exhibited differing occurrences of direct interaction with NADPH, ranging from low to moderate prevalence, with cumulative frequencies of 0.3, 0.4, 0.5, 0.7, respectively. However, these interactions increased significantly when accounting for water molecule-bridging between these residues and the phosphate groups, resulting in combined frequencies of 0.6, 0.7, 0.9, 1.0, respectively.

3.2. *Effects of the coenzyme and the quaternary state on the conformational flexibility of PTGR1*

To evaluate how the coenzyme and dimeric state affect PTGR1's conformational dynamics, we generated trajectories for the apo dimer and the NADPH-bound monomer under the same conditions used for the holo dimer. Fig. 6 illustrates that both systems displayed motion trends of the catalytic domain relative to the NADPH-binding domain as seen in the holo dimer. However, narrower opening shifts were observed in the

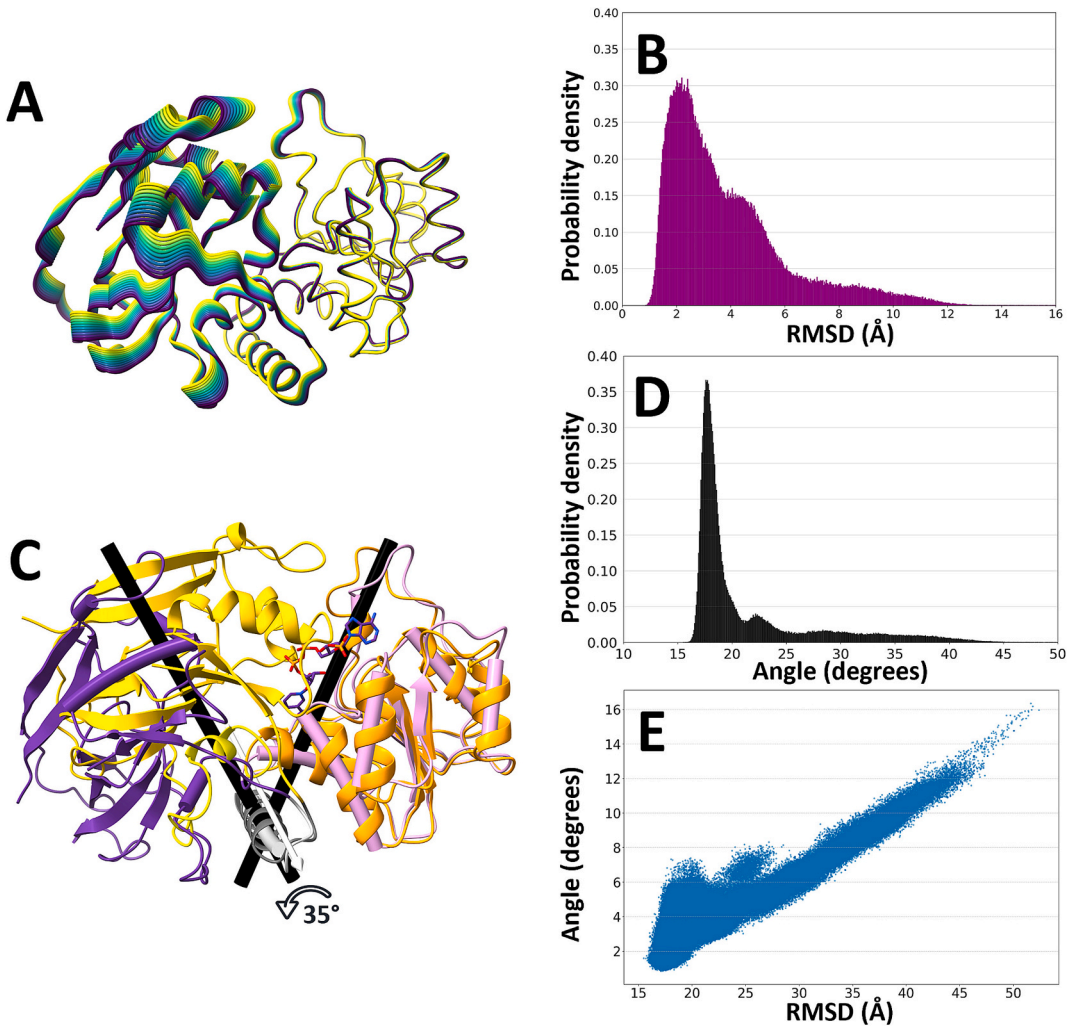

Fig. 3. Conformational fluctuations between the catalytic and NADPH-binding domains of PTGR1. **A.** Depiction of the magnitude of motions along the first PC of the Cα atoms across the concatenated trajectory. **B.** RMSD probability densities of the catalytic domain (residues 1–122, 297–329) relative to the nucleotide-binding domain (residues 123–276). **C.** Representative open and closed conformations of PTGR1, with the open conformation corresponding to snapshots with the largest RMSD. The angle between two vectors (black cylinders) was defined to describe the enzyme's opening. The center of mass of the Cα atoms of residues 277–292 was used as the pivot, while residues 11–18 and 242–248 were taken as reference for the other end of the catalytic and nucleotide-binding domain vectors, respectively. **D.** Angle probability densities. **E.** Correlation between the opening angle and RMSD values. The data presented corresponds to the combined analysis of the two protomers of the PTGR1 dimer, using the last 350 ns of the five replicates simulated at 310 K, pH 7.4.

RMSD and angle data, particularly in the NADPH-depleted dimer. In the apo dimer, the dominant angle peak centered at ~17.5°, corresponding to the closed conformation of the holo dimer, became even more populated. A secondary peak centered at ~27° was detected. In contrast, the NADPH-bound monomer displayed more appreciable variations relative to the holo dimer. The RMSD and angle densities for the closed state decreased, while intermediate conformations (RMSD ~4.5 Å, angle ~19.3°) between the closed and semi-open forms of the holo dimer were more frequently sampled. The FELs of each system revealed distinct distributions (Fig. SI-5 A,B). Variance along the first principal component was even more constrained in the apo dimer than in the NADPH-bound monomer, indicating a greater restriction in conformational flexibility relative to the holo dimer (Fig. SI-5C). Three discernible clusters were identified for the apo dimer, all resembling the closed-like conformation of the holo dimer (Fig. SI-5 A). In contrast, the NADPH-bound monomer formed only two clusters, both representing intermediate states between the closed and semi-open conformation of the holo dimer (Fig. SI-5B). These findings suggest that both NADPH and interchain interactions modulate the conformational flexibility of PTGR1, emphasizing their importance for the functional adaptability of the enzyme.

Correlated movement analysis provided additional insights into PTGR1's domain organization (Fig. 7). By aligning trajectories to the hinge domain's axis of rotation, we observed a strong positive correlation within residues of both the catalytic domain and the nucleotide-binding site, confirming that each region moves as a cohesive unit (Fig. 7A). Conversely, a slight negative correlation between the two domains suggested a marginal degree of dependence, with each domain tending to move in opposite directions. Similar patterns were observed in the apo dimer and NADPH-bound monomer (Fig. 7B,C); however, the apo dimer showed somewhat stronger correlations between the catalytic and nucleotide-binding domains, while they diminished in the monomer. In terms of intersubunit communication, NADPH binding enhanced the coordination between NADPH-binding domains across protomers in the dimer, a coordination weakened in the apo form (Fig. 7D,E). In contrast, the catalytic domains showed no direct correlation with each other, but each displayed a moderate positive correlation with the opposite subunit's binding domain, patterns unaffected by NADPH presence. Together, these findings indicate that both the coenzyme and oligomeric state significantly impact intra and intersubunit

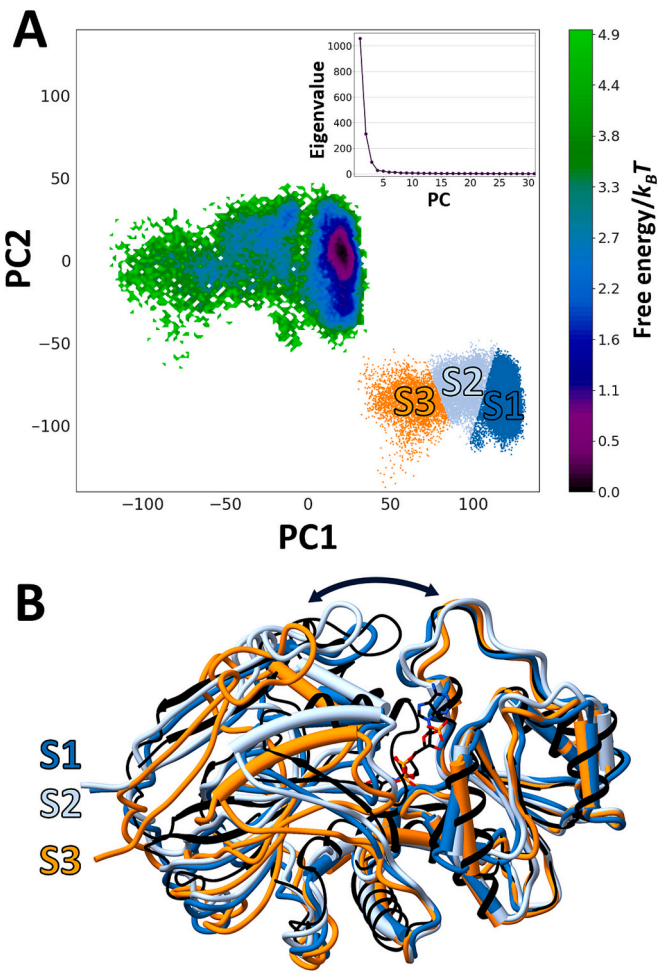

Fig. 4. Free energy landscapes of PTGR1. **A.** FEL (in k_BT units) was obtained from a Cartesian PCA projected onto the first two principal components for a trajectory aligned to the NADPH-binding domain. The clusters identified via a k-means analysis are depicted in the bottom-right corner of the plot. **Inset:** Eigenvalue distributions for the first 20 eigenvectors. **B.** Representative structures of the three clusters. S1 includes the closed conformers of the enzyme, S2 contains the semi-open conformers, and S3 encompasses the most open conformers. The centroid of each state is shown in cylinder representation, colored according to the k-means cluster visualization shown in panel **A**, and superimposed on the reference structure in black ribbons. The data presented corresponds to the combined analysis of the two protomers of the PTGR1 dimer, using the last 350 ns of the five replicates simulated at 310 K, pH 7.4.

communication within PTGR1, influencing its dynamic behavior.

3.3. Covalent binding of LicA to PTGR1

To investigate the potential site and mode of binding of LicA, we conducted virtual molecular covalent docking of the inhibitor onto PTGR1, followed by subsequent unconstrained MD simulations of the resulting complex. An essential element guiding this analysis was the experimental discovery demonstrating LicA's cross-linking with the thiol group of C^{239} of PTGR1, a residue integral to the NADPH-binding site [27]. Topology and parameter files of a modified Cys residue were constructed, where the sulfur atom was covalently attached to the C_β atom of LicA (Table SI-2), thereby simulating the product of a Michael addition reaction within the NAPDH's cavity of PTGR1. The virtual docking results demonstrated a high degree of consistency among the poses, revealing only two distinct groups with slightly different orientations among the top-scoring poses (Fig. 8).

To assess whether LicA modifies the conformational space of PTGR1, MD simulations of the covalent adduct, analogous to those performed with the NADPH complex, were conducted. For these simulations, we used the LicA pose with the lowest energy, which in turn belonged to the predominant binding mode among the top-ranked covalent poses. A combined analysis of both enzyme protomers is summarized in Fig. 9. Each of the three domains continued to behave as a cohesive structural unit, although a second minor peak shifted towards somewhat larger RMSD values was evident for the catalytic domain (Fig. 9A). Regarding the opening motion (Fig. 9B), the RMSD analysis revealed a single broad peak centered around ~4 Å, accompanied by a notable decrease in the frequency of conformations with RMSD values >8 Å observed in the holo dimer. In contrast, the angle distribution identified three distinct populations with varying degrees of interdomain opening: one cluster centered at 17.5° (representing the closed state of the holo dimer), another at 23.6° (corresponding to the semi-open state of the holo dimer), and a dominant cluster at 19.1°, which represents an intermediate opening state only populated by the NADPH-bound monomer (Fig. 6D). Like the RMSD results, the angle distribution revealed that the extent of opening in the covalent adduct was significantly smaller than that observed in the holo dimer. In line with these findings, a single-state FEL was obtained (Fig. SI-6 A), with the eigenvalue for PC1 significantly smaller than that of the NADPH-bound dimer (Fig. SI-6B). The centroid of this state exhibited a slightly more open conformation than the closed state of the holo dimer (Fig. SI-6C), with an opening angle of ~19°. Cross-correlation maps revealed distinct intra- and intersubunit displacement patterns compared to those observed in the apo or holo dimers (Fig. SI-7). Additionally, the presence of LicA induced localized structural changes, characterized by the rupture of certain interdomain contacts and the formation of new contacts involving residues in the region adjacent to the inhibitor (Fig. 9D, Table SI-3). In summary, the covalent binding of LicA substantially altered the conformational dynamics of PTGR1, stabilizing a distinctive state that features a group of non-native contacts. This state exhibited an NADPH-site opening intermediate between the S1 and S2 states of the holo dimer, along with a significant reduction in the extent of the maximum opening motions.

3.4. Noncovalent binding of LicA to PTGR1

To evaluate the stereochemical complementarity, and thus the specificity, of LicA recognition by PTGR1 prior to covalent binding, we conducted a noncovalent virtual docking between the two molecules. To strengthen the docking results, we first characterized the solvation properties of the NADPH-binding site using the MDmix method. This approach involves MD simulations in mixed solvent box containing water and an organic cosolvent. Ethanol was chosen as the cosolvent due to its proven stereochemistry, allowing for identification of preferential interaction sites on the protein with both polar (via its hydroxyl group) and hydrophobic groups (via its methyl group) found in drug-like molecules [58,59,66].

Fig. 10A reveals multiple solvation sites (SS) that were observed for both ethanol and water molecules on the surface of the NADPH-binding site in the absence of the coenzyme. Notably, there was a continual influx and efflux of solvent molecules into the binding site. Five preferential SS ($\Delta G \leq -0.7$ kcal/mol) were identified, two corresponding to the methyl group (SS_{CT1} and SS_{CT2}), and one to the hydroxyl group (SS_{OH}) of ethanol, while the remaining two were attributed to water molecules (SS_{WAT1} and SS_{WAT2}). SS_{CT1} was positioned within a hydrophobic pocket where the nicotinamide moiety of NADPH anchors. This SS was surrounded by residues M^{124}, T^{128}, V^{154}, C^{239}, and V^{272}. SS_{WAT1} and SS_{WAT2} occupied positions equivalent to the amide and ribose ether of nicotinamide, respectively. SS_{CT2} and SS_{OH} were in the more polar region of the cavity, responsible for binding the adenine moiety of NADPH. The hydrophobic surfaces of A^{149}, K^{178}, M^{316}, and N^{321} anchored SS_{CT2}. Conversely, SS_{OH} occupied a space corresponding to the α-phosphate of NADPH, interacting with the side chain of N^{321} and the backbone of A^{153}. Furthermore, the analysis revealed several low-energy

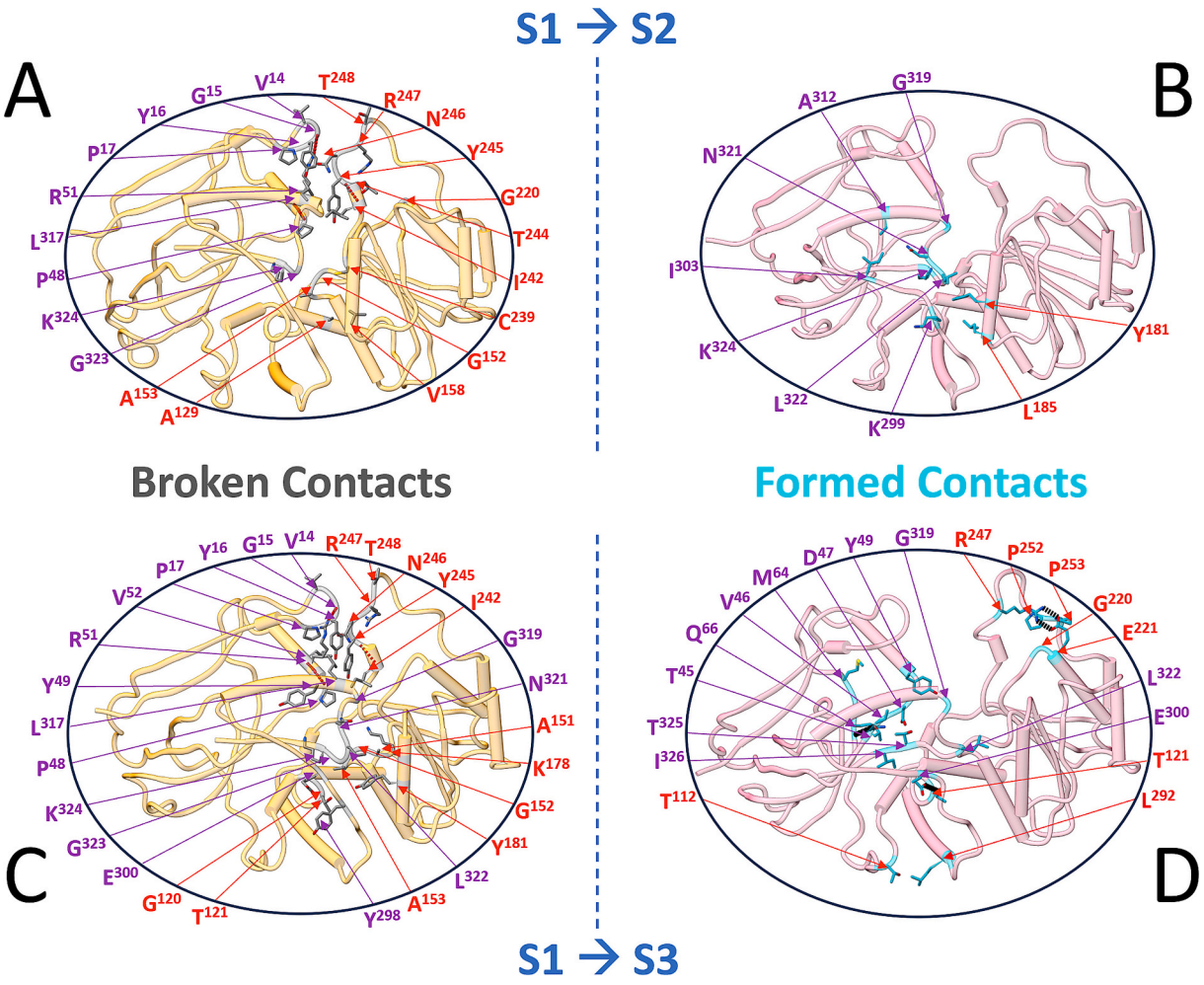

Fig. 5. Residue-residue contact changes across PTGR1 conformational clusters. **A.** Contacts disrupted in the S1➔S2 conformational change. **B.** Newly formed contacts in the S1➔S2 conformational change. **C.** Contacts disrupted in the S1➔S3 conformational change. **D.** Newly formed contacts in the S1➔S3 conformational change. Only contact changes with prevalence shifts greater than 0.5 between the compared macrostates are shown. A cutoff of 5.5 Å was used to identify residue-residue contacts. Quantitative changes for contact prevalences in each state are provided in Table SI-1.

SS_{WAT} ($\Delta G > -0.7$ kcal/mol), closely mirroring the positions occupied by well-defined crystal water molecules. Using these five SS as pharmacophoric guides, we docked NADPH onto PTGR1, achieving a success rate of 0.72 (RMSD <4 Å relative to the experimental pose). In contrast, without using preferential solvation information, the coenzyme pose was correctly predicted with a success rate of only 0.28. This difference in the docking results indicates that the determined SS indeed captured key information underlying the interaction between the enzyme and its coenzyme.

We conducted noncovalent docking of the inhibitor by utilizing the low-energy SS as pharmacophoric guides. Since LicA is smaller and more hydrophobic than NADPH, we constrained the docking process by imposing the use of either hydrophobic SS, while treating the other as an optional element. Additionally, SS_{OH} was set as obligatory, while the two hydration sites were regarded as optional elements. Among the top 100 poses resulting from this docking, we identified two recurring binding modes exhibiting an inverted orientation of LicA. To discern between these two modes, an additional pharmacophoric criterion was applied, requiring that the thiol group of C^{239} be within van der Waals distance from the C_β atom of LicA, i.e., the two chemical groups identified to be cross-linked with each other in the chemoproteomic profiling study [27]. As depicted in Fig. 10B, the resulting pose revealed the LicA's quinolone group in a region akin to where the adenine of NADPH binds. Notably, this pose exhibited closely the same orientation as that obtained with covalent docking, albeit with a slightly greater distance from the thiol group of C^{239} due to the absence of the intermolecular covalent bond. Additionally, the ring carrying the prenyl and methoxy moieties was rotated by ~160°. To investigate the stability of this complex, we conducted unconstrained MD simulations. Three replicates, each spanning 100 ns, were performed, with one LicA molecule (Table SI-4) present in each of the two PTGR1 subunits. The inhibitor's position remained fixed at the designated sites throughout all replicates. The prenyl group, exposed to the solvent, exhibited the most mobility within LicA due to the free rotation capability of the single bond connecting it to the ring. A consistent set of binding residues was identified, forming stable interactions with the inhibitor (Fig. 10C). A stable hydrogen bond between the hydroxyl group of Y^{245} and the OH2 of LicA was identified, persisting over 90 % of the cumulative time across the three trajectories of each protomer. Importantly, the distance between the thiol group of C^{239} and the C_β atom of LicA remained within van der Waals distance for most of the simulation. This distance transiently increased, mainly due to the rotation of the side chain of C^{239} (Fig. 10D).

3.5. *The NADPH-binding site of PTGR1 as a specific pharmacological target*

To explore the conservation of the NADPH-binding site in PTGR1, we analyzed the sequences of this enzyme's orthologs. We compiled sequences from 530 vertebrate species available in the GenBank and conducted a multiple alignment. With this information, we generated a

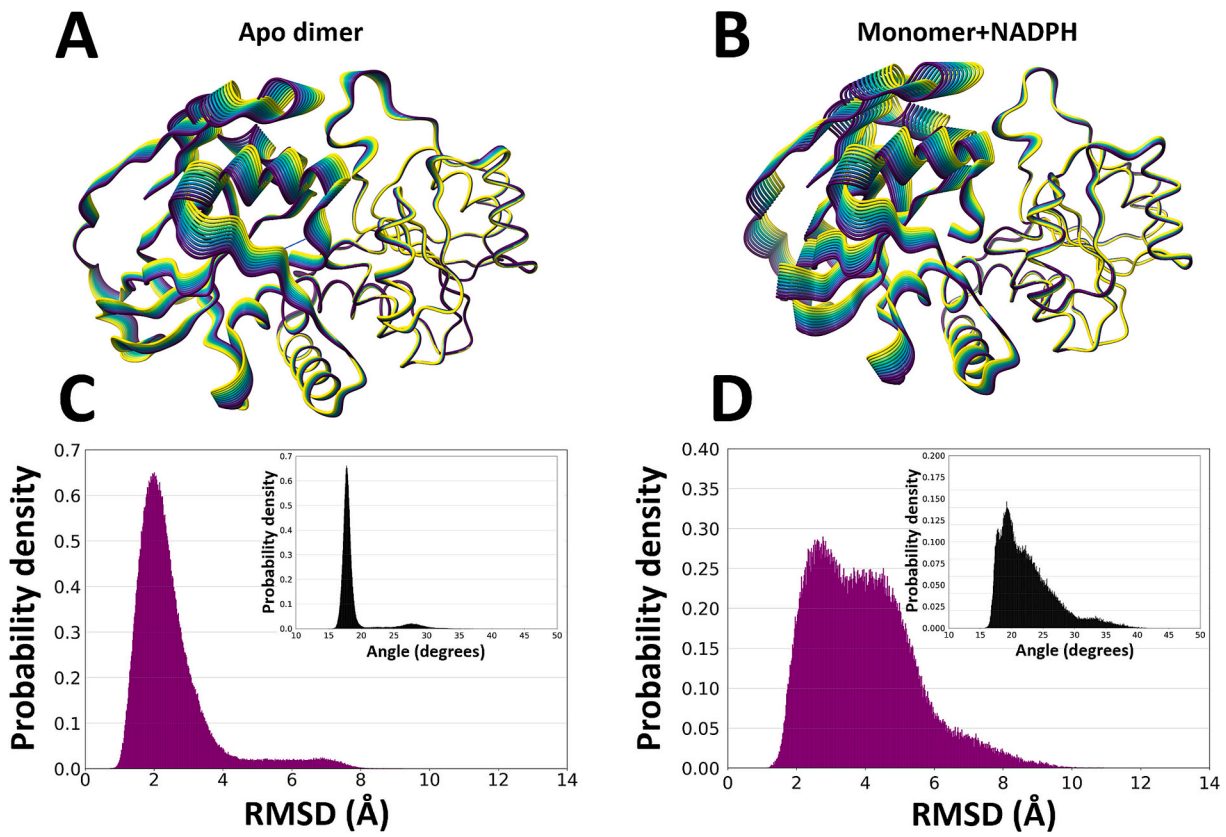

Fig. 6. Conformational fluctuations between the catalytic and NADPH-binding domains of PTGR1 in the apo form (left panels) and in monomeric state bound to NADPH (right panels). **A,B.** Depiction of the magnitude of motions in the first PC of the Cα atoms throughout the concatenated trajectory. **C,D.** RMSD probability densities of the catalytic domain (residues 1–122, 297–329) relative to the nucleotide-binding domain (residues 123–276). **Insets:** Angle probability densities as defined in Fig. 3's legend.

sequence logo. The residues depicted in Fig. 11 are those situated within 5 Å of the coenzyme in the 3D structure of PTGR1. As evidenced, the NADPH-binding site of PTGR1 orthologues demonstrated a pronounced degree of conservation (Fig. 11A). While this outcome was anticipated, the presence of positions with significant variability stands out, especially in the C-term region. As an alternative approach for investigating the conservation of NADPH-binding sites, we conducted an analysis of residue variability in human proteins that interact with this coenzyme. A search using the Foldseek software identified 474 human proteins with the Rossmann fold motif [67]. From this set, entries containing the keyword 'nicotinamide' were selected, resulting in a subset of 151 unique proteins. Due to the diversity of protein architectures bearing the Rossmann fold motif, structural alignment was performed on residues equivalent to the NADPH-binding site in PTGR1, reducing the subset to 94 entries. Following a multiple alignment, 16 structures were identified with at least 90 % sequence overlap in NADPH-binding residues, showing an average identity of 37 ± 15 %. PTGR2 and PTGR3 had the closest identities at ~83 % and 54 %, respectively, to PTGR1. Finally, with this information, we generated the corresponding sequence logo (Fig. 11B). The results plainly depicted the extensive diversity in the amino acid composition constituting the NADPH-binding site in human proteins [68], even among proteins that share a Rossmann-fold architecture similar to that of PTGR1. A recent comprehensive analysis of orthologs of nine different eukaryotic MDR proteins yielded similar results to those presented in Fig. 10B [10].

4. Discussion

Although PTGR1 shows promise as an anticancer target, its conformational dynamics has remained largely uncharacterized, an essential information for pharmacological modulation of its enzymatic activity. In this study, we performed a comprehensive conformational characterization of human PTGR1 using MD simulations. Our analysis revealed that PTGR1 undergoes conformational transitions between closed and open states, marked by rigid body-like displacements of the catalytic and the nucleotide-binding domains, pivoted by a α-helix hinge region. In the closed conformation, NADPH is located in a deep, relatively solvent-inaccessible cavity. Our simulations revealed that transitions between the closed and open states, which proceed through a semi-open intermediate, are frequent in the submicrosecond timescale. Notably, simulations of the apo dimer and the NADPH-bound monomer revealed that both the enzyme's quaternary structure and the coenzyme binding significantly influence its conformational landscape, enhancing the opening dynamics of the NADPH-binding site. This effect extends to the catalytic site, which is partially shielded from the solvent by residues spanning both the NADPH-binding domain of one subunit and the catalytic domain of the other. Consequently, the dynamic behavior of the holo dimer supports the efficient and rapid turnover of both the coenzyme and substrate/product. Comparable opening and closing motions at the nucleotide-binding site have been proposed for other zinc-independent members of the MDR superfamily, based on crystallographic studies of apo and holo enzyme forms [69,79–81] and MD simulations [82]. To our knowledge, however, this is the first study to provide a detailed characterization of the conformational landscape of a prostaglandin reductase.

In this study, we performed an in-silico characterization of PTGR1 inhibition by LicA, a secondary metabolite known for its significant antioxidant and anti-inflammatory properties. In contemporary pharmacology, a pivotal goal is the development of molecules with highly specificity for their intended targets, minimizing the likelihood of cross-

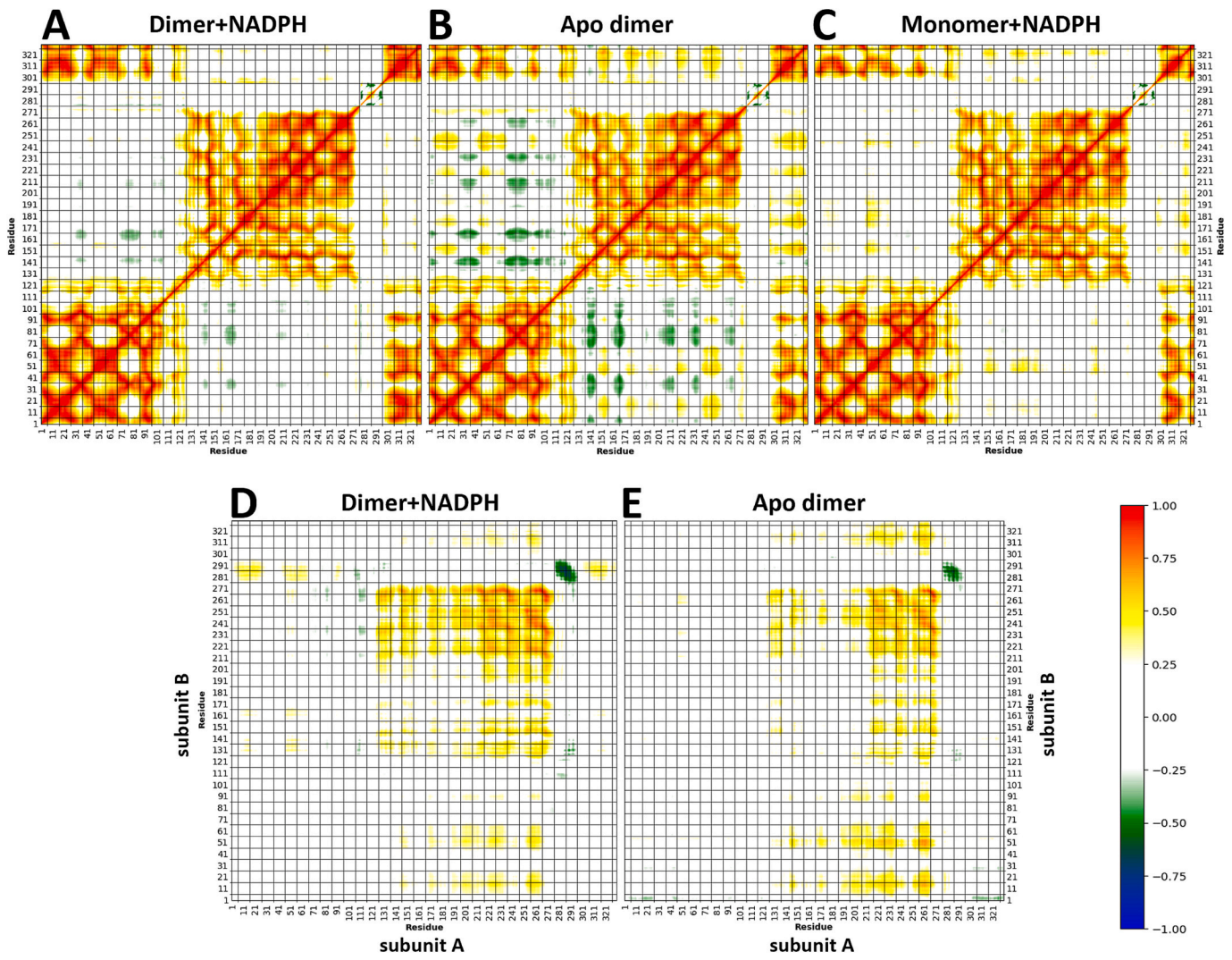

Fig. 7. Dynamic cross-correlation maps for PTGR1 residues. Panels show *intrasubunit* correlations for **(A)** the NADPH-bound dimer, **(B)** the apo dimer, and **(C)** the NADPH-bound monomer. *Intersubunit* correlations are shown for **(D)** the NADPH-bound dimer and **(E)** the apo dimer. Color-coding from blue to white to red indicates the degree of correlated (positive) and anti-correlated (negative) motions. (For interpretation of the references to color in this figure legend, the reader is referred to the web version of this article.)

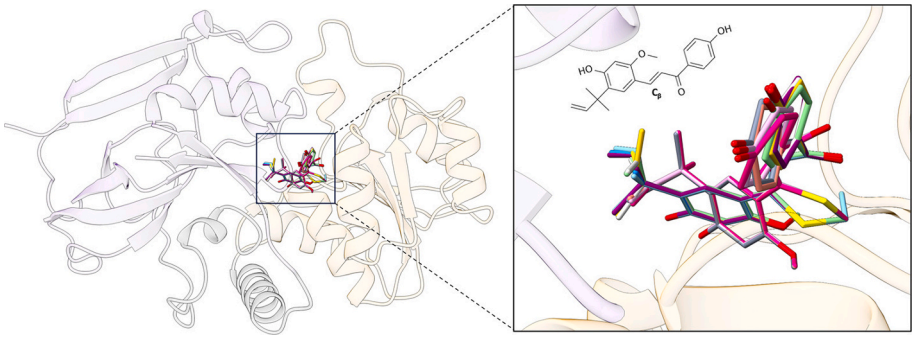

Fig. 8. Covalent docking of LicA onto the NADPH site of PTGR1. The ten top-ranked poses of LicA covalently bound to Cys^{239} are shown superimposed. Covalent docking was performed with AutoDock4 v4.2.6 [60,61].

reactions with off-targets, which are a common cause of adverse drug effects. Integral to achieving this objective is a comprehensive understanding of the structural details governing the interaction between the receptor and the lead molecule. We investigated the potential binding mode of LicA when covalently bound to PTGR1. A crucial aspect in this exploration was the prior experimental observation that this chalcone binds to C^{239}, located in the NADPH-binding site [27]. Virtual docking predicted a highly favored orientation for the inhibitor within the top-ranked poses. MD simulations indicated that PTGR1, with the covalently bound inhibitor, exhibits a more restricted conformational

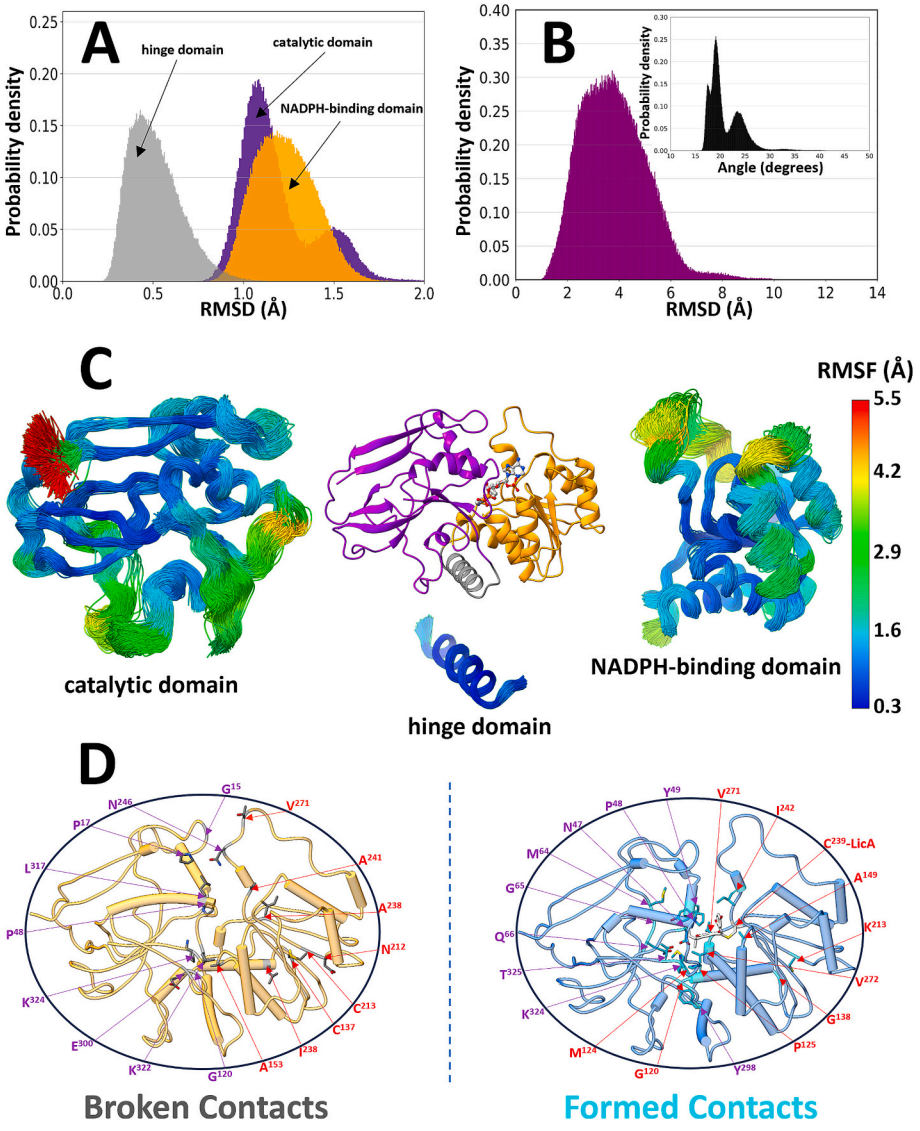

Fig. 9. Conformational flexibility of PTGR1 covalently bound to LicA. **A.** RMSD probability densities, calculated by comparing the coordinates of each domain to those in the initial structure. **B.** RMSD probability densities of the catalytic domain relative to the nucleotide binding domain. **Inset**: Depiction of the magnitude of motions in the first PC of the Cα atoms throughout the concatenated trajectory. **C.** Snapshots from MD trajectories were taken every 50 ns and aligned based on a subset of residues from the corresponding domain with the lowest RMSD. Regions within each snapshot were color-coded by the RMSF values of the backbone's heavy atoms. The RMSF plot is shown in Fig. SI-3. **D.** Differences in contacts between the NADPH-bound S1 state and Lic-A bound enzyme. Disrupted and formed contacts are shown in the S1 (left) and licA-bound centroids, respectively. The data presented corresponds to the combined analysis of the two protomers of the PTGR1 dimer, using the last 350 ns of the five replicates simulated at 310 K and pH 7.4.

landscape, predominantly confined to a slightly more open state than the fully closed conformation. This perturbation highlights the delicate balance underlying the active site opening mechanism of PTGR1.

Before covalent binding can occur, LicA must access the interior of the NADPH-binding cavity and suitable position its C_β atom to react with the thiol group of C^{239}. Therefore, determining whether this approach is facilitated by noncovalent stereochemical complementarity is critical, as this would lay the foundations for achieving specific covalent inhibition. To investigate this, we conducted noncovalent molecular docking of LicA onto PTGR1. To enhance the precision of the docking process, we gained valuable insights into PTGR1's affinity for organic molecules by conducting MD simulations in a water/ethanol solvent. The results revealed multiple solvent sites where water molecules and the hydroxyl and methyl groups of ethanol strongly interacted with the amino acids within the NADPH-binding site. By leveraging these solvent sites, we elucidated a binding mode where the thiol group of C^{239} and the C_β atom of LicA were positioned within van der Waals distance, consistent with the reported chemical cross-linking between these groups. Importantly, the noncovalent pose was strikingly similar to that of the covalently bound inhibitor. In addition, unconstrained MD simulations confirmed the stability of the proposed binding pose of LicA, with the cross-linking groups maintaining proximity throughout the simulations.

Beyond the evolution of the ligand for achieving refined stereochemical complementarity, the recognition site to which it anchors should exhibit distinctive characteristics. These residues, along with selected highly conserved residues, could serve as targets for designing drug-like molecules to attain high binding potency and specificity. Sequence analysis of PTGR1 orthologs in vertebrates revealed a highly conserved NADPH-binding site, with moderate variations, particularly in the C-term segment. In contrast, a comparison of human proteins featuring the Rossmann fold whose 3D structure has been experimentally solved, revealed substantial variability in the composition of the NADPH-binding sites. The nucleotide-binding sites of PTGR2 and PTGR3, the other two prostaglandin reductases compared, exhibit 3 and

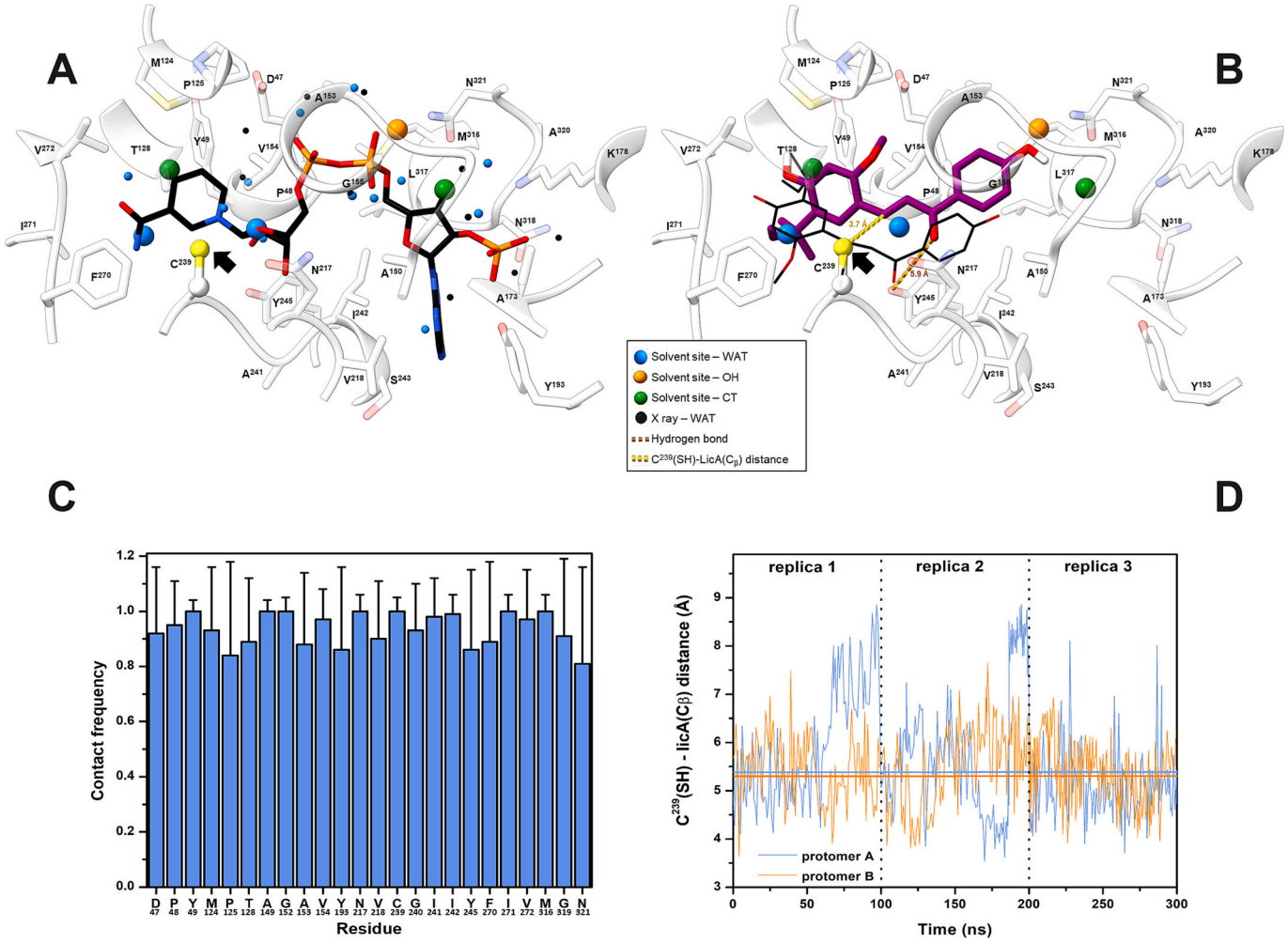

Fig. 10. Solvent sites identification and noncovalent docking of licA on PTGR1's NADPH-binding site. **A.** Hydrophobic and hydrophilic cosolvent sites determined by the MDMix approach (energy < -0.7 kcal/mol) are represented by green and orange spheres, respectively. Hydration sites with interaction energy < -0.7 and > -0.7 kcal/mol are indicated by large and small blue spheres, respectively. NADPH (black sticks) and water molecules (small black spheres) solved in the experimental structure are also shown. **B.** The most energetically favorable solvent sites identified in the NADPH-binding site were used to guide the noncovalent docking of LicA (magenta sticks). For comparison, the covalently docked pose of LicA is shown (black sticks). **C.** Contact frequency of PTGR1 residues with noncovalently docked LicA. Cumulative frequencies for combined three 100-ns MD simulations of the two protomers. **D.** Distance variation over time between the thiol group of C^{239} and the C_β atom of LicA. The results are depicted in a concatenated format for the three MD simulation replicates, with individual runs separated by horizontal dotted lines. Results for each protomer in the dimer are shown. Colored solid horizontal lines depict the average distances for each site. MD simulations of PTGR1 were carried out in a water/ethanol mixture box. (For interpretation of the references to color in this figure legend, the reader is referred to the web version of this article.)

11 mutations, respectively, relative to PTGR1. Notably, C^{239} is a relatively poorly conserved residue among proteins with an NADPH binding site, which would hinder covalent binding to LicA. Supporting the specificity of LicA for PTGR1, the chemoproteomic analysis conducted by Roberts et al. [27] detected, within the limits of experimental resolution, exclusive cross-linking between these molecules. However, it is worth mentioning that PTGR2, the enzyme most similar to PTGR1, does have a cysteine residue in the equivalent position.

Covalent drugs offer significant therapeutic advantages but also come with certain drawbacks. One major disadvantage is their potential for unexpected toxicity and hypersensitivity reactions due to their high reactivity, which can lead to off-target interactions or adverse effects in essential physiological pathways. This concern has historically limited their development, although advances in selective targeting have made covalent drugs safer and more widely used [83,84]. While evidence suggests that LicA can interact with other human proteins [85], the promising perspective is that, through rational design and evolution of its chemical structure, molecules can be developed with the desired ability to selectively bind to human PTGR1.

CRediT authorship contribution statement

Sara Abigail Ramírez-Cortés: Writing – review & editing, Methodology, Investigation, Formal analysis, Conceptualization. **Adrián Durán-Vargas:** Writing – review & editing, Investigation, Formal analysis. **Jesús Antonio Rauda-Ceja:** Writing – review & editing, Visualization, Investigation. **Paola Mendoza-Espinosa:** Writing – review & editing, Investigation, Formal analysis. **Luis Fernando Cofas-Vargas:** Writing – review & editing, Investigation, Formal analysis. **Armando Cruz-Rangel:** Writing – review & editing, Writing – original draft, Methodology, Investigation, Formal analysis, Conceptualization. **Julio Isael Pérez-Carreón:** Writing – review & editing, Investigation, Formal analysis. **Enrique García-Hernández:** Writing – review & editing, Writing – original draft, Supervision, Resources, Methodology, Formal analysis, Conceptualization.

Declaration of competing interest

The authors declare that they have no known competing financial

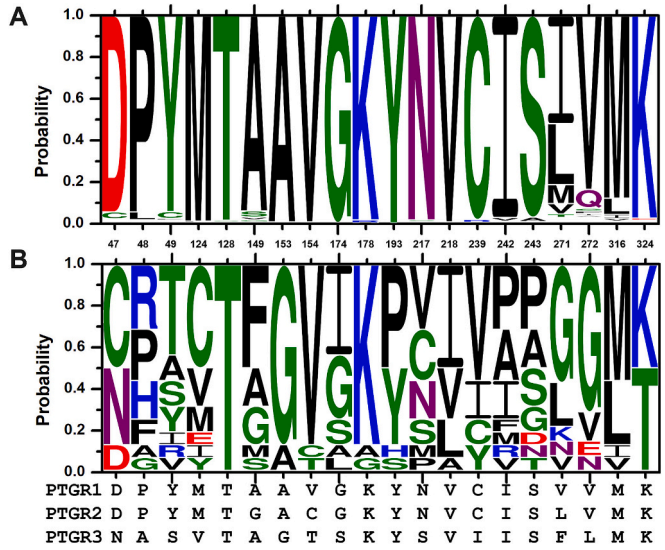

Fig. 11. Conservation of the NADPH-binding site**.** Residue numbering on the x-axis corresponds to the human PTGR1 sequence. **A.** Vertebrate PTGR1 sequences. **B.** Human NADPH-binding sequences. In this last case, the following human NADPH-binding proteins bearing a Rossmann-fold domain were retrieved from the PDB with the indicated identity percentage with respect to PTGR1: PTGR1 (100 %, PDB ID 2Y05), PTGR2 (83 %, PDB ID 2ZB8 [69]), PTGR3 (54 %, PDB ID 2C0C), σ alcohol dehydrogenase (27 %, PDB ID 1AGN, [70]), α alcohol dehydrogenase (27 %, PDB ID 1HSO, [71]), β1 alcohol dehydrogenase (27 %, PDB ID 1HSZ, [72]), γ2 alcohol dehydrogenase (27 %, PDB ID 1HT0, [72]), β3 alcohol dehydrogenase (27 %, PDB ID 1HTB, [73]), χχ alcohol dehydrogenase (27 %, PDB ID 1HTB, [74]), ζ crystallin (32 %, PDB ID 1YB5, to be published), glutathione-dependent formaldehyde dehydrogenase (32 %, PDB ID 2FZW, [75]), P53 inducible oxidoreductase (38 %, PDB ID 2J8Z, [76]), reticulon 4 interacting protein 1 (35 %, PDB ID 2VN8), class II alcohol dehydrogenase (32 %, PDB ID 3COS), vesicle amine transport-1 (38 %, PDB ID 6LHR, [77]), fatty acid synthase (38 %, PDB ID 8EYI, [78]).

interests or personal relationships that could have appeared to influence the work reported in this paper.

Acknowledgements

A.R.-C. is a doctoral student from Programa de Doctorado en Ciencias Biomédicas, A.D.-V. and J.A.R.-C. are doctoral students from Programa de Doctorado en Ciencias Bioquímicas, and A.C.-R. is a doctoral student from Programa de Doctorado en Ciencias Biológicas, from Universidad Nacional Autónoma de México (UNAM), and received Ph. D. fellowships from CONAHCyT. This work was financed in part by DGAPA, UNAM [PAPIIT, IN209624].

Appendix A. Supplementary data

Supplementary data to this article can be found online at https://doi.org/10.1016/j.bpc.2025.107410.

Data availability

We have used the AMBER22 MD simulation package to perform all the simulations. Software packages can be found as indicated: AMBER at https://ambermd.org/GetAmber.php; MDLovotif at https://m3g.github.io/mdlovofit/; MDmix at https://github.com/CBDD/pyMDmix; DynDom at https://dyndom.cmp.uea.ac.uk/dyndom/main.jsp; rDock at https://github.com/CBDD/rDock. Analysis codes are available at https://github.com/egarciahkiki/2024-PTGR1.git. The MD trajectories are openly available at https://zenodo.org/records/14028319

References

[1] J. Mesa, C. Alsina, U. Oppermann, X. Parés, J. Farrés, S. Porté, Human prostaglandin reductase 1 (PGR1): substrate specificity, inhibitor analysis and site-directed mutagenesis, Chem. Biol. Interact. 234 (2015) 105–113, https://doi.org/10.1016/j.cbi.2015.01.021.

[2] T. Hori, J. Ishijima, T. Yokomizo, H. Ago, T. Shimizu, M. Miyano, Crystal structure of anti-configuration of indomethacin and leukotriene B4 12-Hydroxydehydrogenase/15-Oxo-prostaglandin 13-reductase complex reveals the structural basis of broad spectrum indomethacin efficacy, J. Biochem. 140 (2006) 457–466, https://doi.org/10.1093/jb/mvj176.

[3] T. Yokomizo, T. Izumi, T. Takahashi, T. Kasama, Y. Kobayashi, F. Sato, Y. Taketani, T. Shimizu, Enzymatic inactivation of leukotriene B4 by a novel enzyme found in the porcine kidney. Purification and properties of leukotriene B4 12-hydroxydehydrogenase, J. Biol. Chem. 268 (1993) 18128–18135, https://doi.org/10.1016/S0021-9258(17)46820-7.

[4] X. Wang, G. Yin, W. Zhang, K. Song, L. Zhang, Z. Guo, Prostaglandin reductase 1 as a potential therapeutic target for Cancer therapy, Front. Pharmacol. 12 (2021) 717730, https://doi.org/10.3389/fphar.2021.717730.

[5] X.-Z. Ding, R. Hennig, T.E. Adrian, Lipoxygenase and cyclooxygenase metabolism: new insights in treatment and chemoprevention of pancreatic cancer, Mol. Cancer 2 (2003) 10, https://doi.org/10.1186/1476-4598-2-10.

[6] Z.-J. Liu, Y.-J. Sun, J. Rose, Y.-J. Chung, C.-D. Hsiao, W.-R. Chang, I. Kuo, J. Perozich, R. Lindahl, J. Hempel, B.-C. Wang, The first structure of an aldehyde dehydrogenase reveals novel interactions between NAD and the Rossmann fold, Nat. Struct. Biol. 4 (1997) 317–326, https://doi.org/10.1038/nsb0497-317.

[7] H. Riveros-Rosas, A. Julián-Sánchez, R. Villalobos-Molina, J.P. Pardo, E. Piña, Diversity, taxonomy and evolution of medium-chain dehydrogenase/reductase superfamily, Eur. J. Biochem. 270 (2003) 3309–3334, https://doi.org/10.1046/j.1432-1033.2003.03704.x.

[8] T. Hori, T. Yokomizo, H. Ago, M. Sugahara, G. Ueno, M. Yamamoto, T. Kumasaka, T. Shimizu, M. Miyano, Structural basis of leukotriene B4 12-Hydroxydehydrogenase/15-Oxo-prostaglandin 13-reductase catalytic mechanism and a possible Src homology 3 domain binding loop, J. Biol. Chem. 279 (2004) 22615–22623, https://doi.org/10.1074/jbc.M312655200.

[9] D.A. Vitturi, C.-S. Chen, S.R. Woodcock, S.R. Salvatore, G. Bonacci, J.R. Koenitzer, N.A. Stewart, N. Wakabayashi, T.W. Kensler, B.A. Freeman, F.J. Schopfer, Modulation of nitro-fatty acid signaling, J. Biol. Chem. 288 (2013) 25626–25637, https://doi.org/10.1074/jbc.M113.486282.

[10] L.J. Östberg, J.-O. Höög, B. Persson, Computational analysis of human medium-chain dehydrogenases/reductases revealing substrate- and coenzyme-binding characteristics, Chem. Biol. Interact. 390 (2024) 110876, https://doi.org/10.1016/j.cbi.2024.110876.

[11] B. Persson, J. Hedlund, H. Jörnvall, Medium- and short-chain dehydrogenase/reductase gene and protein families, Cell. Mol. Life Sci. 65 (2008) 3879, https://doi.org/10.1007/s00018-008-8587-z.

[12] H. Riveros-Rosas, A. Julián-Sánchez, R. Villalobos-Molina, J.P. Pardo, E. Piña, Diversity, taxonomy and evolution of medium-chain dehydrogenase/reductase superfamily, Eur. J. Biochem. 270 (2003) 3309–3334, https://doi.org/10.1046/j.1432-1033.2003.03704.x.

[13] L.J. Östberg, J.-O. Höög, B. Persson, Computational analysis of human medium-chain dehydrogenases/reductases revealing substrate- and coenzyme-binding characteristics, Chem. Biol. Interact. 390 (2024) 110876, https://doi.org/10.1016/j.cbi.2024.110876.

[14] T. Hori, T. Yokomizo, H. Ago, M. Sugahara, G. Ueno, M. Yamamoto, T. Kumasaka, T. Shimizu, M. Miyano, Structural basis of leukotriene B4 12-Hydroxydehydrogenase/15-Oxo-prostaglandin 13-reductase catalytic mechanism and a possible Src homology 3 domain binding loop, J. Biol. Chem. 279 (2004) 22615–22623, https://doi.org/10.1074/jbc.M312655200.

[15] R.A. Dick, M.-K. Kwak, T.R. Sutter, T.W. Kensler, Antioxidative function and substrate specificity of NAD(P)H- dependent Alkenal/one oxidoreductase, J. Biol. Chem. 276 (2001) 40803–40810, https://doi.org/10.1074/jbc.M105487200.

[16] R.A. Dick, T.W. Kensler, The catalytic and kinetic mechanisms of NADPH-dependent Alkenal/one oxidoreductase, J. Biol. Chem. 279 (2004) 17269–17277, https://doi.org/10.1074/jbc.M400427200.

[17] R. Sánchez-Rodríguez, J.E. Torres-Mena, V. Quintanar-Jurado, V. Chagoya-Hazas, E. Rojas del Castillo, L. del Pozo Yauner, S. Villa-Treviño, J.I. Pérez-Carreón, Ptgr1 expression is regulated by NRF2 in rat hepatocarcinogenesis and promotes cell proliferation and resistance to oxidative stress, Free Radic. Biol. Med. 102 (2017) 87–99, https://doi.org/10.1016/j.freeradbiomed.2016.11.027.

[18] Y. Zhao, C.-C. Weng, M. Tong, J. Wei, H.-H. Tai, Restoration of leukotriene B4-12-hydroxydehydrogenase/15- oxo-prostaglandin 13-reductase (LTBDH/PGR) expression inhibits lung cancer growth in vitro and in vivo, Lung Cancer 68 (2010) 161–169, https://doi.org/10.1016/j.lungcan.2009.06.011.

[19] L. Xue, Z. Zhu, Z. Wang, H. Li, P. Zhang, Z. Wang, Q. Chen, H. Chen, T. Chong, Knockdown of prostaglandin reductase 1 (PTGR1) suppresses prostate cancer cell proliferation by inducing cell cycle arrest and apoptosis, Biosci. Trends 10 (2016) 133–139, https://doi.org/10.5582/bst.2016.01045.

[20] L. Tapak, M. Saidijam, M. Sadeghifar, J. Poorolajal, H. Mahjub, Competing risks data analysis with high-dimensional covariates: an application in bladder cancer, Genom. Proteom. Bioinform. 13 (2015) 169–176, https://doi.org/10.1016/j.gpb.2015.04.001.

[21] M. Liu, Y. Liu, L. Deng, D. Wang, X. He, L. Zhou, M.S. Wicha, F. Bai, S. Liu, Transcriptional profiles of different states of cancer stem cells in triple-negative breast cancer, Mol. Cancer 17 (2018) 65, https://doi.org/10.1186/s12943-018-0809-x.

[22] C.B. Clish, Y.-P. Sun, C.N. Serhan, Identification of dual cyclooxygenase–eicosanoid oxidoreductase inhibitors: NSAIDs that inhibit PG-LX reductase/LTB4 dehydrogenase, Biochem. Biophys. Res. Commun. 288 (2001) 868–874, https://doi.org/10.1006/bbrc.2001.5841.
[23] S.-H. Kim, M. Yang, J.-G. Xu, X. Yu, X.-J. Qian, Role of licochalcone A on thymic stromal lymphopoietin expression: implications for asthma, Exp. Biol. Med. 240 (2015) 26–33, https://doi.org/10.1177/1535370214545020.
[24] N. Song, J.-E. Kim, J. Park, J. Kim, H. Kang, E. Lee, Y.-G. Kang, J. Son, S. Seo, Y. Heo, K. Lee, Licochalcone A, a polyphenol present in licorice, suppresses UV-induced COX-2 expression by targeting PI3K, MEK1, and B-Raf, Int. J. Mol. Sci. 16 (2015) 4453–4470, https://doi.org/10.3390/ijms16034453.
[25] R. Wu, X.-Y. Li, W.-H. Wang, F.-F. Cai, X.-L. Chen, M.-D. Yang, Q.-S. Pan, Q.-L. Chen, R.-Y. Zhou, S.-B. Su, Network pharmacology-based study on the mechanism of Bushen-Jianpi decoction in liver Cancer treatment, Evid. Based Complement. Alternat. Med. 2019 (2019) 1–13, https://doi.org/10.1155/2019/3242989.
[26] C. Qiu, T. Zhang, W. Zhang, L. Zhou, B. Yu, W. Wang, Z. Yang, Z. Liu, P. Zou, G. Liang, Licochalcone A inhibits the proliferation of human lung cancer cell lines A549 and H460 by inducing G2/M cell cycle arrest and ER stress, Int. J. Mol. Sci. 18 (2017) 1761, https://doi.org/10.3390/ijms18081761.
[27] L.S. Roberts, P. Yan, L.A. Bateman, D.K. Nomura, Mapping novel metabolic nodes targeted by anti-cancer drugs that impair triple-negative breast cancer pathogenicity, ACS Chem. Biol. 12 (2017) 1133–1140, https://doi.org/10.1021/acschembio.6b01159.
[28] D.A. Case, H.M. Aktulga, K. Belfon, I.Y. Ben-Shalom, J.T. Berryman, S.R. Brozell, R. M. Betz, D.S. Cerutti, I.T.E. Cheatham, G.A. Cisneros, V.W.D. Cruzeiro, T. A. Darden, R.E. Duke, G. Giambasu, H. Gilson, H. Gohlke, A.W. Goetz, R. Harris, S. Izadi, S.A. Izmailov, K. Kasavajhala, M.C. Kaymak, E. King, A. Kovalenko, T. Kurtzman, T.S. Lee, S. LeGrand, P. Li, C. Lin, J. Liu, T. Luchko, R. Luo, M. Machado, M. Man, M. Manathunga, K.M. Merz, Y. Miao, O. Mikhailovskii, G. Monard, H. Nguyen, K.A. O'Hearn, A. Onufriev, F. Pan, S. Pantano, R. Qi, A. Rahnamoun, D.R. Roe, A. Roitbert, C. Sagui, S. Schott-Verdugo, A. Shajan, J. Shen, C.L. Simmerling, N.R. Skrynnikiv, J. Smith, J. Swails, R.C. Walker, J. Wang, J. Wang, H. Wei, R.M. Wolf, X. Wu, Y. Xiong, Y. Xue, D.M. York, S. Zhao, P.A. Kollman, Amber 22, University of California, San Francisco, 2022.
[29] S. Izadi, R. Anandakrishnan, A.V. Onufriev, Building water models: a different approach, J. Phys. Chem. Lett. 5 (2014) 3863–3871, https://doi.org/10.1021/jz501780a.
[30] R. Salomon-Ferrer, D.A. Case, R.C. Walker, An overview of the Amber biomolecular simulation package, Wiley Interdiscip. Rev. Comput. Mol. Sci. 3 (2013) 198–210, https://doi.org/10.1002/wcms.1121.
[31] C. Tian, K. Kasavajhala, K.A.A. Belfon, L. Raguette, H. Huang, A.N. Migues, J. Bickel, Y. Wang, J. Pincay, Q. Wu, C. Simmerling, ff19SB: amino-acid-specific protein backbone parameters trained against quantum mechanics energy surfaces in solution, J. Chem. Theory Comput. 16 (2020) 528–552, https://doi.org/10.1021/acs.jctc.9b00591.
[32] P.L. Cummins, K. Ramnarayan, U.C. Singh, J.E. Gready, Molecular dynamics/free energy perturbation study on the relative affinities of the binding of reduced and oxidized NADP to dihydrofolate reductase, J. Am. Chem. Soc. 113 (1991) 8247–8256, https://doi.org/10.1021/ja00022a008.
[33] P. Eastman, J. Swails, J.D. Chodera, R.T. McGibbon, Y. Zhao, K.A. Beauchamp, L.-P. Wang, A.C. Simmonett, M.P. Harrigan, C.D. Stern, R.P. Wiewiora, B.R. Brooks, V.S. Pande, OpenMM 7: rapid development of high performance algorithms for molecular dynamics, PLoS Comput. Biol. 13 (2017) e1005659, https://doi.org/10.1371/journal.pcbi.1005659.
[34] P. Eastman, J. Swails, J.D. Chodera, R.T. McGibbon, Y. Zhao, K.A. Beauchamp, L. P. Wang, A.C. Simmonett, M.P. Harrigan, C.D. Stern, R.P. Wiewiora, B.R. Brooks, V.S. Pande, OpenMM 7: rapid development of high performance algorithms for molecular dynamics, PLoS Comput. Biol. 13 (2017), https://doi.org/10.1371/JOURNAL.PCBI.1005659.
[35] C.W. Hopkins, S. Le Grand, R.C. Walker, A.E. Roitberg, Long-time-step molecular dynamics through hydrogen mass repartitioning, J. Chem. Theory Comput. 11 (2015) 1864–1874, https://doi.org/10.1021/ct5010406.
[36] T. Darden, D. York, L. Pedersen, Particle mesh Ewald: an N ·log(N) method for Ewald sums in large systems, J. Chem. Phys. 98 (1993) 10089–10092, https://doi.org/10.1063/1.464397.
[37] A.C. Simmonett, B.R. Brooks, A compression strategy for particle mesh Ewald theory, J. Chem. Phys. 154 (2021) 54112.
[38] D.J. Sindhikara, S. Kim, A.F. Voter, A.E. Roitberg, Bad seeds sprout perilous dynamics: stochastic thermostat induced trajectory synchronization in biomolecules, J. Chem. Theory Comput. 5 (2009) 1624–1631, https://doi.org/10.1021/ct800573m.
[39] J. Åqvist, P. Wennerström, M. Nervall, S. Bjelic, B.O. Brandsdal, Molecular dynamics simulations of water and biomolecules with a Monte Carlo constant pressure algorithm, Chem. Phys. Lett. 384 (2004) 288–294, https://doi.org/10.1016/j.cplett.2003.12.039.
[40] J.P. Ryckaert, G. Ciccotti, H.J.C. Berendsen, Numerical integration of the cartesian equations of motion of a system with constraints: molecular dynamics of n-alkanes, J. Comput. Phys. 23 (1977) 327–341, https://doi.org/10.1016/0021-9991(77)90098-5.
[41] L.F. Cofas-Vargas, P. Mendoza-Espinosa, L.P. Avila-Barrientos, D. Prada-Gracia, H. Riveros-Rosas, E. García-Hernández, Exploring the druggability of the binding site of aurovertin, an exogenous allosteric inhibitor of FOF1-ATP synthase, Front. Pharmacol. 13 (2022) 1012008, https://doi.org/10.3389/fphar.2022.1012008.
[42] J.L. Medrano-Cerano, L.F. Cofas-Vargas, E. Leyva, J.A. Rauda-Ceja, M. Calderón-Vargas, P. Cano-Sánchez, G. Titaux-Delgado, C.M. Melchor-Meneses, A. Hernández-Arana, F. del Río-Portilla, E. García-Hernández, Decoding the mechanism governing the structural stability of wheat germ agglutinin and its isolated domains: a combined calorimetric, NMR, and MD simulation study, Protein Sci. 33 (2024) e5020, https://doi.org/10.1002/pro.5020.
[43] J. Wang, W. Wang, P.A. Kollman, D.A. Case, Automatic atom type and bond type perception in molecular mechanical calculations, J. Mol. Graph. Model. 25 (2006) 247–260, https://doi.org/10.1016/j.jmgm.2005.12.005.
[44] X. He, V.H. Man, W. Yang, T.-S. Lee, J. Wang, A fast and high-quality charge model for the next generation general AMBER force field, J. Chem. Phys. 153 (2020), https://doi.org/10.1063/5.0019056.
[45] A. Jakalian, D.B. Jack, C.I. Bayly, Fast, efficient generation of high-quality atomic charges. AM1-BCC model: II. Parameterization and validation, J. Comput. Chem. 23 (2002) 1623–1641, https://doi.org/10.1002/jcc.10128.
[46] E.F. Pettersen, T.D. Goddard, C.C. Huang, E.C. Meng, G.S. Couch, T.I. Croll, J. H. Morris, T.E. Ferrin, U.C.S.F. ChimeraX, Structure visualization for researchers, educators, and developers, Protein Sci. 30 (2021) 70–82, https://doi.org/10.1002/pro.3943.
[47] E.C. Meng, T.D. Goddard, E.F. Pettersen, G.S. Couch, Z.J. Pearson, J.H. Morris, T. E. Ferrin, U.C.S.F. ChimeraX, Tools for structure building and analysis, Protein Sci. 32 (2023) e4792, https://doi.org/10.1002/PRO.4792.
[48] D.R. Roe, T.E. Cheatham, PTRAJ and CPPTRAJ: software for processing and analysis of molecular dynamics trajectory data, J. Chem. Theory Comput. 9 (2013) 3084–3095, https://doi.org/10.1021/ct400341p.
[49] W. McKinney, Data structures for statistical computing in python, in: Proceedings of the 9th Python in Science Conference, 2010, pp. 56–61, https://doi.org/10.25080/Majora-92bf1922-00a.
[50] J.D. Hunter, Matplotlib: A 2D graphics environment, Comput. Sci. Eng. 9 (2007) 90–95, https://doi.org/10.1109/MCSE.2007.55.
[51] M. Waskom, seaborn: statistical data visualization, J. Open Source Softw. 6 (2021) 3021, https://doi.org/10.21105/joss.03021.
[52] L. Martínez, Automatic identification of Mobile and rigid substructures in molecular dynamics simulations and fractional structural fluctuation analysis, PLoS ONE 10 (2015) e0119264, https://doi.org/10.1371/journal.pone.0119264.
[53] S. Hayward, R.A. Lee, Improvements in the analysis of domain motions in proteins from conformational change: DynDom version 1.50, J. Mol. Graph. Model. 21 (2002) 181–183, https://doi.org/10.1016/S1093-3263(02)00140-7.
[54] R.A. Estabrook, J. Luo, M.M. Purdy, V. Sharma, P. Weakliem, T.C. Bruice, N. O. Reich, Statistical coevolution analysis and molecular dynamics: identification of amino acid pairs essential for catalysis, Proc. Natl. Acad. Sci. 102 (2005) 994–999, https://doi.org/10.1073/pnas.0409128102.
[55] T. Ichiye, M. Karplus, Collective motions in proteins: A covariance analysis of atomic fluctuations in molecular dynamics and normal mode simulations, proteins: structure, Funct. Genet. 11 (1991) 205–217, https://doi.org/10.1002/prot.340110305.
[56] S.A.M. Stein, A.E. Loccisano, S.M. Firestine, J.D. Evanseck, Chapter 13 principal components analysis: A review of its application on molecular dynamics data, Annu. Rep. Comput. Chem. 2 (2006) 233–261, https://doi.org/10.1016/S1574-1400(06)02013-5.
[57] M.K. Scherer, B. Trendelkamp-Schroer, F. Paul, G. Pérez-Hernández, M. Hoffmann, N. Plattner, C. Wehmeyer, J.-H. Prinz, F. Noé, PyEMMA 2: A software package for estimation, validation, and analysis of Markov models, J. Chem. Theory Comput. 11 (2015) 5525–5542, https://doi.org/10.1021/acs.jctc.5b00743.
[58] D. Alvarez-Garcia, X. Barril, Molecular simulations with solvent competition quantify water displaceability and provide accurate interaction maps of protein binding sites, J. Med. Chem. 57 (2014) 8530–8539, https://doi.org/10.1021/jm5010418.
[59] L.P. Avila-Barrientos, L.F. Cofas-Vargas, G. Agüero-Chapin, E. Hernández-García, S. Ruiz-Carmona, N.A. Valdez-Cruz, M. Trujillo-Roldán, J. Weber, Y.B. Ruiz-Blanco, X. Barril, E. García-Hernández, Computational design of inhibitors targeting the catalytic β subunit of *Escherichia coli* FOF1-ATP synthase, Antibiotics 11 (2022) 557, https://doi.org/10.3390/antibiotics11050557.
[60] G. Bianco, S. Forli, D.S. Goodsell, A.J. Olson, Covalent docking using autodock: two-point attractor and flexible side chain methods, Protein Sci. 25 (2016) 295–301, https://doi.org/10.1002/pro.2733.
[61] G.M. Morris, R. Huey, W. Lindstrom, M.F. Sanner, R.K. Belew, D.S. Goodsell, A. J. Olson, AutoDock4 and AutoDockTools4: automated docking with selective receptor flexibility, J. Comput. Chem. 30 (2009) 2785–2791, https://doi.org/10.1002/jcc.21256.
[62] S. Ruiz-Carmona, D. Alvarez-Garcia, N. Foloppe, A.B. Garmendia-Doval, S. Juhos, P. Schmidtke, X. Barril, R.E. Hubbard, S.D. Morley, rDock: A fast, versatile and open source program for docking ligands to proteins and nucleic acids, PLoS Comput. Biol. 10 (2014) e1003571, https://doi.org/10.1371/journal.pcbi.1003571.
[63] A. Bateman, M.-J. Martin, S. Orchard, M. Magrane, R. Agivetova, S. Ahmad, E. Alpi, E.H. Bowler-Barnett, R. Britto, B. Bursteinas, H. Bye-A-Jee, R. Coetzee, A. Cukura, A. Da Silva, P. Denny, T. Dogan, T. Ebenezer, J. Fan, L.G. Castro, P. Garmiri, G. Georghiou, L. Gonzales, E. Hatton-Ellis, A. Hussein, A. Ignatchenko, G. Insana, R. Ishtiaq, P. Jokinen, V. Joshi, D. Jyothi, A. Lock, R. Lopez, A. Luciani, J. Luo, Y. Lussi, A. MacDougall, F. Madeira, M. Mahmoudy, M. Menchi, A. Mishra, K. Moulang, A. Nightingale, C.S. Oliveira, S. Pundir, G. Qi, S. Raj, D. Rice, M. R. Lopez, R. Saidi, J. Sampson, T. Sawford, E. Speretta, E. Turner, N. Tyagi, P. Vasudev, V. Volynkin, K. Warner, X. Watkins, R. Zaru, H. Zellner, A. Bridge, S. Poux, N. Redaschi, L. Aimo, G. Argoud-Puy, A. Auchincloss, K. Axelsen, P. Bansal, D. Baratin, M.-C. Blatter, J. Bolleman, E. Boutet, L. Breuza, C. Casals-Casas, E. de Castro, K.C. Echioukh, E. Coudert, B. Cuche, M. Doche, D. Dornevil, A. Estreicher, M.L. Famiglietti, M. Feuermann, E. Gasteiger, S. Gehant,

V. Gerritsen, A. Gos, N. Gruaz-Gumowski, U. Hinz, C. Hulo, N. Hyka-Nouspikel, F. Jungo, G. Keller, A. Kerhornou, V. Lara, P. Le Mercier, D. Lieberherr, T. Lombardot, X. Martin, P. Masson, A. Morgat, T.B. Neto, S. Paesano, I. Pedruzzi, S. Pilbout, L. Pourcel, M. Pozzato, M. Pruess, C. Rivoire, C. Sigrist, K. Sonesson, A. Stutz, S. Sundaram, M. Tognolli, L. Verbregue, C.H. Wu, C.N. Arighi, L. Arminski, C. Chen, Y. Chen, J.S. Garavelli, H. Huang, K. Laiho, P. McGarvey, D. A. Natale, K. Ross, C.R. Vinayaka, Q. Wang, Y. Wang, L.-S. Yeh, J. Zhang, P. Ruch, D. Teodoro, D. Teodoro, UniProt: the universal protein knowledgebase in 2021, Nucleic Acids Res. 49 (2021) D480–D489, https://doi.org/10.1093/nar/gkaa1100.

[64] F. Sievers, A. Wilm, D. Dineen, T.J. Gibson, K. Karplus, W. Li, R. Lopez, H. McWilliam, M. Remmert, J. Söding, J.D. Thompson, D.G. Higgins, Fast, scalable generation of high-quality protein multiple sequence alignments using clustal omega, Mol. Syst. Biol. 7 (2011) 539, https://doi.org/10.1038/msb.2011.75.

[65] C. Girdlestone, S. Hayward, The DynDom3D webserver for the analysis of domain movements in multimeric proteins, J. Comput. Biol. 23 (2016) 21–26, https://doi.org/10.1089/cmb.2015.0143.

[66] J.P. Arcon, L.A. Defelipe, C.P. Modenutti, E.D. López, D. Alvarez-Garcia, X. Barril, A.G. Turjanski, M.A. Martí, Molecular dynamics in mixed solvents reveals protein–ligand interactions, improves docking, and allows accurate binding free energy predictions, J. Chem. Inf. Model. 57 (2017) 846–863, https://doi.org/10.1021/acs.jcim.6b00678.

[67] M. van Kempen, S.S. Kim, C. Tumescheit, M. Mirdita, J. Lee, C.L.M. Gilchrist, J. Söding, M. Steinegger, Fast and accurate protein structure search with Foldseek, Nat. Biotechnol. (2023), https://doi.org/10.1038/s41587-023-01773-0.

[68] Y.H. Hua, C.Y. Wu, K. Sargsyan, C. Lim, Sequence-motif detection of NAD(P)-binding proteins: discovery of a unique antibacterial drug target, Sci. Rep. 4 (2014) 6471, https://doi.org/10.1038/srep06471.

[69] Y.-H. Wu, T.-P. Ko, R.-T. Guo, S.-M. Hu, L.-M. Chuang, A.H.-J. Wang, Structural basis for catalytic and inhibitory mechanisms of human prostaglandin reductase PTGR2, Structure 16 (2008) 1714–1723, https://doi.org/10.1016/j.str.2008.09.007.

[70] P. Xie, S.H. Parsons, D.C. Speckhard, W.F. Bosron, T.D. Hurley, X-ray structure of human class IV ςς alcohol dehydrogenase, J. Biol. Chem. 272 (1997) 18558–18563, https://doi.org/10.1074/jbc.272.30.18558.

[71] T.D. Hurley, W.F. Bosron, C.L. Stone, L.M. Amzel, Structures of three human β alcohol dehydrogenase variants, J. Mol. Biol. 239 (1994) 415–429, https://doi.org/10.1006/jmbi.1994.1382.

[72] M.S. Niederhut, B.J. Gibbons, S. Perez-Miller, T.D. Hurley, Three-dimensional structures of the three human class I alcohol dehydrogenases, Protein Sci. 10 (2001) 697–706, https://doi.org/10.1110/ps.45001.

[73] G.J. Davis, W.F. Bosron, C.L. Stone, K. Owusu-Dekyi, T.D. Hurley, X-ray structure of human β3β3 alcohol dehydrogenase, J. Biol. Chem. 271 (1996) 17057–17061, https://doi.org/10.1074/jbc.271.29.17057.

[74] Z.-N. Yang, W.F. Bosron, T.D. Hurley, Structure of human χχ alcohol dehydrogenase: a glutathione-dependent formaldehyde dehydrogenase, J. Mol. Biol. 265 (1997) 330–343, https://doi.org/10.1006/jmbi.1996.0731.

[75] P.C. Sanghani, W.I. Davis, L. Zhai, H. Robinson, Structure−function relationships in human glutathione-dependent formaldehyde dehydrogenase. Role of Glu-67 and Arg-368 in the catalytic mechanism, Biochemistry 45 (2006) 4819–4830, https://doi.org/10.1021/bi052554q.

[76] S. Porté, E. Valencia, E.A. Yakovtseva, E. Borràs, N. Shafqat, J.É. Debreczeny, A.C. W. Pike, U. Oppermann, J. Farrés, I. Fita, X. Parés, Three-dimensional structure and enzymatic function of Proapoptotic human p53-inducible Quinone oxidoreductase PIG3, J. Biol. Chem. 284 (2009) 17194–17205, https://doi.org/10.1074/jbc.M109.001800.

[77] S.-Y. Kim, T. Mori, M.F. Chek, S. Furuya, K. Matsumoto, T. Yajima, T. Ogura, T. Hakoshima, Structural insights into vesicle amine transport-1 (VAT-1) as a member of the NADPH-dependent quinone oxidoreductase family, Sci. Rep. 11 (2021) 2120, https://doi.org/10.1038/s41598-021-81409-y.

[78] S.M.N. Hasan, J.W. Lou, A.F.A. Keszei, D.L. Dai, M.T. Mazhab-Jafari, Atomic model for core modifying region of human fatty acid synthase in complex with Denifanstat, Nat. Commun. 14 (2023) 3460, https://doi.org/10.1038/s41467-023-39266-y.

[79] F. Colonna-Cesari, D. Perahia, M. Karplus, H. Eklund, C.I. Brädén, O. Tapia, Interdomain motion in liver alcohol dehydrogenase. Structural and energetic analysis of the hinge bending mode, J. Biol. Chem. 261 (1986) 15273–15280, https://doi.org/10.1016/S0021-9258(18)66863-2.

[80] I. Levin, R. Schwarzenbacher, D. McMullan, P. Abdubek, E. Ambing, T. Biorac, J. Cambell, J.M. Canaves, H. Chiu, X. Dai, A.M. Deacon, M. DiDonato, M. Elsliger, A. Godzik, C. Grittini, S.K. Grzechnik, E. Hampton, L. Jaroszewski, C. Karlak, H. E. Klock, E. Koesema, A. Kreusch, P. Kuhn, S.A. Lesley, T.M. McPhillips, M. D. Miller, A. Morse, K. Moy, J. Ouyang, R. Page, K. Quijano, R. Reyes, A. Robb, E. Sims, G. Spraggon, R.C. Stevens, H. van den Bedem, J. Velasquez, J. Vincent, F. von Delft, X. Wang, B. West, G. Wolf, Q. Xu, K.O. Hodgson, J. Wooley, I. A. Wilson, Crystal structure of a putative NADPH-dependent oxidoreductase (GI: 18204011) from mouse at 2.10 Å resolution, Proteins Struct. Funct. Bioinform. 56 (2004) 629–633, https://doi.org/10.1002/prot.20163.

[81] I.G. Shabalin, E.V. Filippova, K.M. Polyakov, E.G. Sadykhov, T.N. Safonova, T. V. Tikhonova, V.I. Tishkov, V.O. Popov, Structures of the apo and holo forms of formate dehydrogenase from the bacterium *Moraxella* sp. C-1: towards understanding the mechanism of the closure of the interdomain cleft, Acta Crystallogr. D Biol. Crystallogr. 65 (2009) 1315–1325, https://doi.org/10.1107/S0907444909040773.

[82] B. Ling, S. Bi, M. Sun, Z. Jing, X. Li, R. Zhang, Molecular dynamics simulations of mutated *Mycobacterium tuberculosis* l-alanine dehydrogenase to illuminate the role of key residues, J. Mol. Graph. Model. 50 (2014) 61–70, https://doi.org/10.1016/j.jmgm.2014.03.008.

[83] F. Sutanto, M. Konstantinidou, A. Dömling, Covalent inhibitors: a rational approach to drug discovery, RSC Med. Chem. 11 (2020) 876–884, https://doi.org/10.1039/D0MD00154F.

[84] L. Boike, N.J. Henning, D.K. Nomura, Advances in covalent drug discovery, Nat. Rev. Drug Discov. 21 (2022) 881–898, https://doi.org/10.1038/s41573-022-00542-z.

[85] A. Okuda-Tanino, D. Sugawara, T. Tashiro, M. Iwashita, Y. Obara, T. Moriya, C. Tsushima, D. Saigusa, Y. Tomioka, K. Ishii, N. Nakahata, Licochalcones extracted from Glycyrrhiza inflata inhibit platelet aggregation accompanied by inhibition of COX-1 activity, PLoS ONE 12 (2017) e0173628, https://doi.org/10.1371/journal.pone.0173628.